R. & M. No. 3706

MINISTRY OF DEFENCE (PROCUREMENT EXECUTIVE)

AERONAUTICAL RESEARCH COUNCIL

REPORTS AND MEMORANDA

Theoretical Use of Variable Porosity in Slotted Tunnels for Minimizing Wall Interference on Dynamic Measurements

By H. C. GARNER

Aerodynamics Dept., R.A.E. Farnborough

LONDON: HER MAJESTY'S STATIONERY OFFICE

1972

PRICE £1·90 NET

Theoretical Use of Variable Porosity in Slotted Tunnels for Minimizing Wall Interference on Dynamic Measurements

By H. C. GARNER

Aerodynamics Dept., R.A.E. Farnborough

Reports and Memoranda No. 3706*

February 1971

Summary

In parallel with a recent experimental study of the use of slotted tunnel liners with variable perforated screens to give interference-free aerodynamic damping derivatives, the corresponding problem is considered theoretically. The principle, that wall interference usually changes sign when slots in the roof and floor of a rectangular tunnel are completely sealed, has prompted these complementary studies with systematic variation of a porosity parameter that can govern the intermediate wall conditions. A theory for small frequency parameter and subsonic compressible flow, which has already explained serious interference effects observed experimentally, is extended to the more general tunnel boundary conditions.

With the aid of a special similarity rule for compressible flow, the six necessary interference parameters are determined by a judicious amalgam of exact and approximate data for incompressible flow, including allowance for elliptic loading over a finite wing span. The corrections to oscillatory lift and pitching moment are formulated. By iterative calculation the theoretical method is applied to pitching motion of the unswept tapered and cropped delta planforms chosen for the related half-model experiments. The most favourable wall porosity for low interference is similar in theory and experiment for the two wings. A recommended practical procedure for approximating to interference-free wall conditions is thus corroborated by theoretical calculation and is also extended to give residual corrections.

The extended procedure is illustrated for the larger cropped delta half-model. It is concluded that the uncertainties from ventilated wall interference on pitching derivatives can be reduced to about 5 per cent of the in-phase lift derivative, provided that the model span does not exceed 40 per cent of the tunnel breadth, nor the planform area 15 per cent of the working cross section. Theory and experiment combine to show that the optimum ventilated wall is hardly influenced by Mach number, so that there are good prospects of eliminating the major interference effects at transonic speeds.

* Replaces RAE Technical Report 71017—ARC 33 053.

LIST OF CONTENTS

1. Introduction

The need for theoretical study of wall interference on oscillating models in ventilated tunnels has continued since the publication of Ref. 1 (Garner, Moore and Wight, 1966). Although that paper gives a mathematical explanation of the serious interference effects on pitching derivatives observed experimentally, it does not provide a complete remedy. Under conditions of small frequency parameter and small model area ratio, satisfactory interference corrections can be applied if the slotted or perforated walls are sealed; with such a configuration blockage or choking would prohibit transonic operation. Under the same model conditions but with open slots in the roof and floor of the tunnel, the wall interference can be formulated satisfactorily unless the slots are too narrow or have perforated screens; unfortunately, the corrections in this case are liable to be of the same order of magnitude as the measurements, and cannot be applied with confidence. One remedy, suggested in Ref. 1, is to reduce the interference effects by having the side-walls ventilated but the roof and floor solid; however, operation at transonic and low supersonic speeds would impose severe limitations on model size to avoid interference due to reflected waves from the solid walls. In order to approximate to interference-free measurements over the operative speed range, it is best to utilize the result that wall interference usually changes sign when slots are completely sealed. This principle has led to experimental and theoretical studies with systematic variation of a porosity parameter that can govern the intermediate wall conditions.

In a series of experimental papers by Moore and Wight[2,3,4] (1967 to 1969), considerable progress has been achieved towards the elimination of interference effects on half-model testing. It is shown in Ref. 2 that, if wall effects are present in a ventilated tunnel at subsonic speeds, they are likely to persist throughout the low supersonic range. It is, therefore, necessary to remove as much of the interference as possible at subsonic speeds; then an empirical method, with $\beta = 0{\cdot}45$ as suggested in Ref. 2, can reasonably be used to correct the measurements at transonic speeds. The investigation in Ref. 2 reveals a systematic influence of the side-wall boundary layer where the half-model is mounted. A simple method of allowing for the displacement thickness of the boundary layer is suggested in Ref. 3, so that an experimental interference-free datum is established from measurements on a cropped-delta half-model tested in three relatively-large ventilated tunnels. The same model has also been tested in the smaller NPL $9\frac{1}{2}$ in $\times$ $9\frac{1}{2}$ in (24 cm $\times$ 24 cm) tunnel with longitudinally slotted liners fitted with perforated screens of adjustable hole size. As the porosity of the screens is changed, the measured oscillatory pitching moment passes through the interference-free datum to define an optimum wall condition that is practically independent of Mach number in the subsonic range. This conclusion is reached in Ref. 3, but a full account of the experiment is given in Ref. 4, which includes similar measurements on an unswept tapered half-wing. Pitching derivatives for the latter planform are known to be sensitive to slotted-wall interference; nevertheless, the same wall condition is found to give measurements in fair agreement with those obtained when the slots are sealed and corrections are made by the method of Ref. 1.

The variable porosity parameter, associated with the perforated screen, is determined from the rate of change of mass flow through the slot with respect to the pressure drop across the ventilated wall in steady flow. Calibration against Mach number is made for four sizes of perforation in Ref. 4, but has not played a crucial part in the subsequent analysis. However, the Appendix to Ref. 4 discusses the interpretation of the quantity P_E from experiment as a porosity parameter in the boundary condition for a slotted-perforated wall. This provides the vital link between experiment and theory. In the present report the theory for small frequency parameter has been extended to the more general boundary condition in subsonic compressible flow. With interference parameters from approximate numerical analysis, theoretical interference-free conditions are found to be reasonably consistent with those from experiment. This result offers the possibility of residual wall corrections when, in Ref. 4 for example, there is no choice of perforated screen that will eliminate interference effects on damping and stiffness derivatives simultaneously.

2. Treatment of Slotted–Perforated Walls

Fig. 1 shows the working section of the NPL $9\frac{1}{2}$ in $\times$ $9\frac{1}{2}$ in (24 cm $\times$ 24 cm) tunnel and the identical spanwise extent of the cropped delta and unswept tapered half-models. The origin O is indicated on the

side-wall, but is regarded as a point on the central axis of a rectangular tunnel of the given height h and an effective breadth b. The side-wall or reflection plane is denoted by $y = 0$ and, including the small gap g, the half-model has spanwise extent $0 \leqslant y \leqslant s$; the z-axis is vertically upwards and, to complete a right-handed system, the x-axis out of the paper represents the direction of the undisturbed stream of velocity U, subsonic Mach number M and density ρ.

The wing is made to oscillate harmonically with angular frequency ω. The perturbation velocity potential is written in the usual form

$$\phi = \text{real part of } \{\bar{\phi}(x, y, z)\, e^{i\omega t}\}. \tag{1}$$

Then the linearized flow is governed by the complex differential equation

$$\beta^2 \frac{\partial^2 \bar{\phi}}{\partial x^2} + \frac{\partial^2 \bar{\phi}}{\partial y^2} + \frac{\partial^2 \bar{\phi}}{\partial z^2} - \frac{2i\omega M^2}{U} \frac{\partial \bar{\phi}}{\partial x} + \frac{\omega^2 M^2 \bar{\phi}}{U^2} = 0, \tag{2}$$

where $\beta^2 = 1 - M^2$. It is assumed that the complex potential $\bar{\phi}_m$ due to the model alone is known in terms of the oscillatory aerodynamic forces acting on it. Then we write

$$\bar{\phi} = \bar{\phi}_m + \bar{\phi}_i, \tag{3}$$

and the problem is to determine $\bar{\phi}_i$ in the region of the model subject to certain boundary conditions on the tunnel walls.

The effective tunnel has solid walls on the sides $y = \pm \frac{1}{2}b$ and the combination of ten longitudinal slots and perforated screens on the doubled roof and floor $z = \pm \frac{1}{2}h$. The relevant details of slot geometry, width a and spacing d, are given in Fig. 1; the adjustable screens are illustrated in Fig. 2 of Ref. 4. The general boundary condition on $\bar{\phi}$, with arbitrary slot geometry and porosity, is discussed and formulated in Section 2.1. Subject to this condition and small frequency, the treatment of equation (2) is considered in Section 2.2.

2.1. Boundary Conditions

The theoretical treatment of slotted walls is discussed in Section 2 of Ref. 1. Instead of separate conditions on the slots and slats, the mixed boundary is represented by a homogeneous condition, which presupposes that the slots are neither too few in number nor too large in width. The boundary condition for steady flow is that proposed by Baldwin, Turner and Knechtel[5] (1954)

$$\frac{\partial \phi}{\partial x} + \frac{1}{2} Fh \frac{\partial^2 \phi}{\partial x \partial n} + \frac{1}{P} \frac{\partial \phi}{\partial n} = 0, \tag{4}$$

where n is the outward normal distance from the boundary,

$$F = \frac{2d}{\pi h} \log_e \operatorname{cosec} \frac{\pi a}{2d} = 0{\cdot}233 \tag{5}$$

and the porosity parameter P, by allusion to a perforated wall, regulates the pressure drop through the slots from tunnel to plenum chamber in proportion to the outflow. The value of F corresponds to the data in Fig. 1 and is unaffected by the reflection plane. The generalization of equation (4) to oscillatory flow is not certain, but it is plausible to take the boundary condition

$$\left(\frac{\partial}{\partial x} + \frac{i\omega}{U}\right)\left(\bar{\phi} + \frac{1}{2} Fh \frac{\partial \bar{\phi}}{\partial n}\right) + \frac{1}{P} \frac{\partial \bar{\phi}}{\partial n} = 0. \tag{6}$$

There is no physical reason why P should not be complex, but it is taken to be real as there is no positive evidence of any phase lag between pressure drop and outflow. Equation (6) reduces to the accepted linearized boundary conditions in the limiting cases of steady flow ($\omega = 0$) and ideal slots ($P \to \infty$), and in particular to

$$\frac{\partial \bar{\phi}}{\partial n} = 0 \tag{7}$$

on the solid walls, which may be interpreted as either $P \to 0$ or $F \to \infty$.

The slots are thought to be wide enough to prevent much effect of the boundary layer on the wall condition. The porosity parameter P is therefore supposed to relate to the size of hole in the perforated screen. The interpretation of P in compressible flow is not straightforward, but a reasoned discussion of the problem is found in the Appendix to Ref. 4. To be consistent with what is observed at transonic speeds, it is considered necessary to write

$$P = \beta P_E, \tag{8}$$

where P_E is determined experimentally with the tunnel empty. The mean outward mass flow ρv_n per unit area is plotted non-dimensionally against the pressure drop Δp from working section to plenum chamber to give a linear calibration, as illustrated for four hole sizes in Fig. 4 of Ref. 4. The slopes then determine

$$P_E = \frac{2\partial(v_n/U)}{\partial(\Delta p/q)}, \tag{9}$$

where $q = \frac{1}{2}\rho U^2$ is the dynamic pressure of the undisturbed stream. The small, but significant, dependence of P_E on Mach number for each hole size is reproduced in the upper diagram of Fig. 2. With substitution from equation (8), the boundary condition (6) becomes

$$\left(\frac{\partial}{\partial x} + \frac{i\omega}{U}\right)\left(\bar{\phi} + \frac{1}{2}Fh\frac{\partial \bar{\phi}}{\partial n}\right) + \frac{1}{\beta P_E}\frac{\partial \bar{\phi}}{\partial n} = 0. \tag{10}$$

2.2. Similarity Rule for Compressible Flow

The basic principle underlying the simple analytical solutions for wall interference in Ref. 1 is the integral relationship between the steady and oscillatory velocity potentials for incompressible flow in equation (10) of that report. The result is generalized to the case of low-frequency subsonic compressible flow, and there follows a convenient interdependence of the real and imaginary parts of the interference upwash

$$\bar{w}_i = \frac{\partial \bar{\phi}_i}{\partial z}, \tag{11}$$

which continues to hold for ideal slots ($P_E \to \infty$). The principle no longer applies when P_E is finite and non-zero, and we are faced with a formidable combination of differential equation (2) and boundary condition (10).

Some simplification results from the use of the potential function ψ such that

$$\bar{\phi}(x, y, z) = \psi(X, y, z) \exp\left\{\frac{i\omega M^2 X}{\beta U}\right\}, \tag{12}$$

where $X = x/\beta$. Then ψ satisfies the differential equation

$$\frac{\partial^2\psi}{\partial X^2} + \frac{\partial^2\psi}{\partial y^2} + \frac{\partial^2\psi}{\partial z^2} + \frac{\omega^2 M^2\psi}{\beta^2 U^2} = 0, \tag{13}$$

which reduces to Laplace's equation in the limit of small frequency when $O(\omega^2)$ is negligible. The model potential

$$\psi_m = \bar{\phi}_m \exp\left\{-\frac{i\omega M^2 X}{\beta U}\right\}, \tag{14}$$

and hence the corresponding interference potential

$$\psi_i = \psi - \psi_m, \tag{15}$$

both satisfy the same governing differential equation. With substitution from equation (12), the boundary condition (10) becomes

$$\left(\frac{\partial}{\partial X} + \frac{i\Omega}{U}\right)\left(\psi + \frac{1}{2}Fh\frac{\partial\psi}{\partial n}\right) + \frac{1}{P_E}\frac{\partial\psi}{\partial n} = 0, \tag{16}$$

where $\Omega = \omega/\beta$. Thus the interference potential satisfies

$$\left(\frac{\partial}{\partial X} + \frac{i\Omega}{U}\right)\left(\psi_i + \frac{1}{2}Fh\frac{\partial\psi_i}{\partial n}\right) + \frac{1}{P_E}\frac{\partial\psi_i}{\partial n} = -\left(\frac{\partial}{\partial X} + \frac{i\Omega}{U}\right)\left(\psi_m + \frac{1}{2}Fh\frac{\partial\psi_m}{\partial n}\right) - \frac{1}{P_E}\frac{\partial\psi_m}{\partial n} \tag{17}$$

on the roof and floor, while on the solid side-walls ($P_E \to 0$)

$$\frac{\partial\psi_i}{\partial n} = -\frac{\partial\psi_m}{\partial n}. \tag{18}$$

Starting from the elementary perturbation velocity potential of a small area S with lift coefficient C_L at the origin in steady incompressible flow

$$\phi_{m0} = \frac{USC_L z}{8\pi(y^2 + z^2)}\left[1 + \frac{x}{(x^2 + y^2 + z^2)^{\frac{1}{2}}}\right], \tag{19}$$

we use equation (11) of Ref. 1 to construct the corresponding quantity

$$\bar{\phi}_m = \int_{-\infty}^{x/\beta} \exp\left\{\frac{i\omega\xi}{\beta U} - \frac{i\omega x}{U}\right\}\frac{\partial\phi_{m0}}{\partial\xi}\,d\xi \tag{20}$$

in oscillatory compressible flow. By equations (14), (19) and (20) it is easily shown that

$$\psi_m = \frac{USC_L}{8\pi}\int_{-\infty}^{X} \frac{z}{(\xi^2 + y^2 + z^2)^{\frac{3}{2}}} \exp\left\{\frac{i\Omega(\xi - X)}{U}\right\} d\xi. \tag{21}$$

Apart from the substitutions $X = x/\beta$ and $\Omega = \omega/\beta$, equations (17) and (21) are invariant for $M < 1$. With a fixed value of P_E and low frequency, the similarity rule for compressible flow is first to solve for

$$\psi_i = \bar{\phi}_i(x, y, z; \omega, 0) \text{ with } M = 0,$$

and then to take

$$\bar{\phi}_i(x, y, z; \omega, M) = \bar{\phi}_i(x/\beta, y, z; \omega/\beta, 0)\left\{1 + \frac{i\omega M^2 x}{\beta^2 U}\right\}. \tag{22}$$

A necessary condition for the similarity rule is that P_E is real. While this is fundamental, it is of little consequence that P_E shows a minor dependence on Mach number. Theoretical calculations must cover the range of hole size in Fig. 2, and we shall take $P_E = 0{\cdot}3$, $1{\cdot}0$ and $2{\cdot}5$. A convenient porosity parameter for purposes of interpolation is the quantity

$$\Psi = (1 + P_E^{-1})^{-1}, \tag{23}$$

plotted in the lower diagram of Fig. 2. There are limiting values $\Psi = 0$ for a solid boundary and $\Psi = 1$ for an ideal slotted wall, both of which play an important part in the subsequent analysis.

3. Method of Interference Correction

The similarity rule in Section 2.2 has reduced the problem to that of solving Laplace's equation subject to the boundary conditions (17) and (18), where ψ_m is known. A numerical finite-difference technique, known as dynamic relaxation, has been developed by Rushton and Laing[6] (1968) for the case of a small model in steady flow. In Ref. 7 they have extended the treatment to oscillations of low frequency and have applied their method to the present wall configuration in incompressible flow. These results for zero span are discussed in Section 3.1.

The calculations by dynamic relaxation are only approximate, and where analytical solutions are available they have been preferred. Furthermore, the span of the half-models in Fig. 1 is large enough to warrant adjustments to the interference parameters, as derived in Section 3.2. Use is made of Holder's[8] (1963) result for finite wings in rectangular tunnels with ventilated roof and floor and also of various formulae from Refs. 1, 9 and 10 (Table 1).

From equations (11) and (22) the complex interference upwash becomes

$$\bar{w}_i = \left\{1 + \frac{i\omega M^2 x}{\beta^2 U}\right\} \frac{\partial \bar{\phi}_i}{\partial z}(x/\beta, y, z; \omega/\beta, 0). \tag{24}$$

In the most general case, when P_E is finite and non-zero, six interference parameters are needed to define $\partial\bar{\phi}_i/\partial z$ in place of the three in Ref. 1. Some re-formulation of the corrections to pitching derivatives is therefore required in Section 3.3.

3.1. Interference Parameters for Small Wing

It follows from Section 2.2, that the expression for the complex interference upwash in equation (15) of Ref. 1 is no longer valid when there is an arbitrary porosity parameter in the homogeneous boundary condition on the ventilated walls of the tunnel. Instead we write for incompressible flow

$$\bar{w}_i(x) = \frac{US\bar{C}_L}{C}\left[\left\{\delta_0 + \delta_1\frac{x}{h} + \delta_2\left(\frac{x}{h}\right)^2\right\} + \frac{i\omega h}{U}\left\{\delta_0' + \delta_1'\frac{x}{h} + \delta_2'\left(\frac{x}{h}\right)^2\right\} + O\left(\frac{x}{h}\right)^3\right], \tag{25}$$

where $C = bh$ and the complex lift coefficient $\bar{C}_L$ is defined by

$$\text{lift} = \text{real part of } \{\tfrac{1}{2}\rho U^2 S\bar{C}_L\, e^{i\omega t}\}. \tag{26}$$

By equation (24) the corresponding result for compressible flow becomes

$$\bar{w}_i(x) = \frac{US\bar{C}_L}{C}\left[\left\{1 + \frac{i\omega M^2 x}{\beta^2 U}\right\}\left\{\delta_0 + \delta_1\frac{x}{\beta h} + \delta_2\left(\frac{x}{\beta h}\right)^2\right\}\right.$$

$$\left. + \frac{i\omega h}{\beta U}\left\{\delta'_0 + \delta'_1\frac{x}{\beta h} + \delta'_2\left(\frac{x}{\beta h}\right)^2\right\} + O\left(\frac{x}{\beta h}\right)^3\right]. \tag{27}$$

With fixed slot parameter F, the integral for δ'_0 in equation (16) of Ref. 1 and the simplifications

$$\delta_2 = 0, \qquad \delta'_1 = -\delta_0, \qquad \delta'_2 = -\tfrac{1}{2}\delta_1 \tag{28}$$

hold only when $P_E \to 0$ or ∞. In general, all six of the interference parameters from equation (25) need to be determined.

The method of solution in Ref. 7 is to split

$$\bar{\phi} = \bar{\phi}_R + i\bar{\phi}_I \tag{29}$$

into its real and imaginary parts, both of which satisfy Laplace's equation in incompressible flow. Similarly

$$\bar{\phi}_m = \bar{\phi}_{mR} + i\bar{\phi}_{mI} = \frac{US\bar{C}_L}{8\pi}\int_0^\infty \frac{z\, e^{-i\omega x'/U}}{[(x - x')^2 + y^2 + z^2]^{\frac{3}{2}}}\, dx', \tag{30}$$

the interference potential $\bar{\phi}_i$ and the boundary condition (10) are separated into their real and imaginary parts. The components $\bar{\phi}_{iR}$ and $\bar{\phi}_{iI}$ are linked by both parts of the boundary condition on the ventilated roof and floor. A very small value $\omega h/U = 0{\cdot}01$ is substituted into equation (30). Then $\bar{\phi}_m$ and $\partial\bar{\phi}_m/\partial n$ are evaluated on the tunnel walls, and the finite-difference equations for $\bar{\phi}_{iR}$ and $\bar{\phi}_{iI}$ at an array of mesh points are set up and solved by an extension of the dynamic relaxation method of Ref. 6. The results are readily expressed in terms of equation (25); the interference parameters, taken from Table 3 of Ref. 7, are reproduced in Table 2. For fixed $b/h = 2{\cdot}6$ with solid side-walls and $F = 0{\cdot}233$ on the roof and floor, all six interference parameters are tabulated for variable porosity parameter $P = P_E$; the limiting case of an open roof and floor ($F = 1/P = 0$) is also included.

Restrictions on the total of mesh points make it necessary to consider the accuracy of the approximate results from Ref. 7. The analytical result due to Holder[8] in equation (6.73) of Ref. 9 gives

$$\delta_0 = \delta_0^{(1)} - \sum_{k=0}^{\infty} I_k, \tag{31}$$

where $\delta_0^{(1)}$ denotes the value for a closed rectangular tunnel from equation (20) of Ref. 1,

$$I_0 = \frac{1}{2\pi P_E}\int_0^\infty \frac{dq}{(\sinh q + Fq\cosh q)^2 + (P_E^{-1}\cosh q)^2}, \tag{32}$$

and for $k \geqslant 1$

$$I_k = \frac{1}{\pi P_E}\int_0^\infty \frac{dq}{(q/\alpha_k)^2(\sinh\alpha_k + F\alpha_k\cosh\alpha_k)^2 + (P_E^{-1}\cosh\alpha_k)^2} \tag{33}$$

where

$$\alpha_k = [q^2 + (k\pi h/b)^2]^{\frac{1}{2}}.$$

The exact values of δ_0 in Table 2 have been computed from these equations and others listed in Table 1. The plot in Fig. 3 against the porosity parameter Ψ from equation (23) shows that Ref. 7 is least accurate near $\Psi = 0$, that is, when the perforated screens are almost closed. All the interference parameters have been calculated exactly for the limiting case $\Psi = 0$ from equations in Ref. 1 and from the simple relations (28) that also apply to ideal slots ($\Psi = 1$). These exact data have been plotted in Figs. 3 and 4, and it appears that the broken curves from Table 2 must be adjusted in the range $\Psi < 0{\cdot}4$. At the other extreme, open roof and floor, the results from Ref. 7 are accurate within 1 or 2 per cent. It is significant that δ_0, the leading coefficient of the real part of the interference upwash, vanishes at a larger value of Ψ than does the all-important imaginary term in δ_0'.

3.2. Effect of Model Span

Of greater importance than the numerical approximations in Ref. 7, the effect of model span has to be taken into account. We have to consider a breadth to height ratio $b/h = 2{\cdot}6$, and Fig. 17 of Ref. 1 shows how the steady lift interference parameter $(\delta_0)_E$ becomes more sensitive to wing span as b/h increases from 1 to 2.

It follows from equations (6) to (8) of Ref. 8, that for a uniformly loaded wing of span $b\tau$ the spanwise distribution of interference upwash across a rectangular tunnel with ventilated roof and floor is given by

$$\frac{Cw_i(y)}{USC_L} = \delta_0(\eta, \tau)$$

$$= \delta_0^{(1)}(\eta, \tau) - \sum_{k=0}^{\infty} I_k \frac{\cos(k\pi\eta)\sin(k\pi\tau)}{k\pi\tau}, \tag{34}$$

where the first term corresponds to a closed tunnel with the same b/h, $\eta = 2y/b$ and I_k is defined in equations (32) and (33). The general formulation of $(\delta_0)_E$ in equation (3.46) of Ref. 10 may be written as

$$(\delta_0)_E = \frac{16}{\pi^2}\int_0^1\int_0^1 \delta_0(\eta,\tau)\left(\frac{\tau}{\sigma}\right)^2\left\{1-\left(\frac{\tau}{\sigma}\right)^2\right\}^{-\frac{1}{2}}\left\{1-\left(\frac{\eta}{\sigma}\right)^2\right\}^{\frac{1}{2}} d\left(\frac{\tau}{\sigma}\right) d\left(\frac{\eta}{\sigma}\right) \tag{35}$$

where $\sigma = 2s/b$. Its value $(\delta_0^{(1)})_E$ for the closed tunnel is readily calculated from equation (3.84) of Ref. 10. It follows from equations (34) and (35) that

$$(\delta_0)_E = (\delta_0^{(1)})_E - \frac{16}{\pi^2}\sum_{k=0}^{\infty} I_k \int_0^{\frac{1}{2}\pi}\int_0^{\frac{1}{2}\pi} \frac{\cos(k\pi\sigma\sin\phi)\sin(k\pi\sigma\sin\theta)}{k\pi\sigma}\sin\theta\cos^2\phi\, d\theta\, d\phi, \tag{36}$$

where we have substituted $\tau = \sigma\sin\theta$ and $\eta = \sigma\sin\phi$. By separation of the variables θ and ϕ it can be shown that

$$(\delta_0)_E = (\delta_0^{(1)})_E - I_0 - \sum_{k=1}^{\infty} I_k\left[\frac{2J_1(k\pi\sigma)}{k\pi\sigma}\right]^2, \tag{37}$$

which is formally similar to the result in equation (10) of Ref. 8, except that $\sin(k\pi\sigma)$ is replaced by the Bessel function $2J_1(k\pi\sigma)$ in changing from uniform to elliptic spanwise loading. Special care is needed in the evaluation of the integrals for I_k, but once these are known it is relatively simple to compute $(\delta_0)_E$ as a function of σ.

With reference to equations (6.68) of Ref. 9 and (3.17) of Ref. 10, the corresponding result for an ideal slotted roof and floor is

$$(\delta_0)_E = (\delta_0^{(1)})_E - \frac{1}{4(1+F)} - \frac{\pi h}{b}\sum_{k=1}^{\infty}\left\{\frac{k}{\Theta_k e^{2k\pi h/b}-1} + \frac{k}{e^{2k\pi h/b}+1}\right\}\left[\frac{2J_1(k\pi\sigma)}{k\pi\sigma}\right]^2, \tag{38}$$

where

$$\Theta_k = \frac{b + k\pi hF}{b - k\pi hF}.$$

The limiting case of closed side-walls and open roof and floor is obtained by substituting $F = 0$ and $\Theta_k = 1$ in equation (38); it has been checked numerically that this more elegant and convenient formulation is consistent with the method described in equations (63) to (65) of Ref. 1.

The parameter $(\delta_0)_E$ has been evaluated from equations (32), (33), (37) and (38) and plotted against σ in Fig. 5 for $F = 0{\cdot}233$ and five values of $1/P_E$. The present application requires $\sigma = 0{\cdot}385$, when the effect of span is to reduce $\delta_0^{(1)}$ for the closed tunnel by 28 per cent. The values of $(\delta_0)_E$ for $\sigma = 0{\cdot}385$ are used for δ_0 in Table 3; apart from δ_2 and δ_1' for the special cases $1/P_E = 0$ and ∞, there is an element of guesswork in all the other interference parameters. For the closed roof and floor, we have ignored Ref. 7 and applied the correction factor

$$\frac{(\delta_0^{(1)})_E}{\delta_0^{(1)}} = 0{\cdot}722 \tag{39}$$

to the exact values for the small wing plotted in Figs. 3 and 4. For the ideal slotted roof and floor ($1/P_E = 0$), a trivial adjustment has been made to Table 2 before applying the correction factor

$$\frac{(\delta_0)_E}{\delta_0} = 0{\cdot}880 \tag{40}$$

to each interference parameter. For the intermediate cases $1/P_E = 3{\cdot}0$, $1{\cdot}0$ and $0{\cdot}4$, each approximate value in Table 2 has been corrected by an amount

$$\lambda_1 \times (\text{known error when } 1/P_E = \infty)$$

with respective values $\lambda_1 = 0{\cdot}63$, $0{\cdot}11$ and 0. Finally the increment due to $\sigma = 0{\cdot}385$ is calculated to be

$$\lambda_2\,(\text{increment when } 1/P_E = 0) + (1 - \lambda_2)\,(\text{increment when } 1/P_E = \infty),$$

where the respective values $\lambda_2 = 0{\cdot}21$, $0{\cdot}49$ and $0{\cdot}73$ are determined from the exact values of δ_0 and $(\delta_0)_E$. For example, the estimated δ_1 in Table 3 is

$$\delta_1 = (\delta_1)_{\text{Ref. 7}} + \lambda_1[\delta_1^{(1)} - (\delta_1)_{\text{Ref. 7},\infty}] - 0{\cdot}120\lambda_2(\delta_1)_{\text{Ref. 7},0} - 0{\cdot}278(1 - \lambda_2)\delta_1^{(1)}, \tag{41}$$

where $\delta_1^{(1)} = 0{\cdot}3741$, $(\delta_1)_{\text{Ref. 7},\infty} = 0{\cdot}444$ from Table 2 and there is a trivial adjustment in $(\delta_1)_{\text{Ref. 7},0}$ from $-0{\cdot}233$ to $-0{\cdot}236$ to be consistent with the corresponding value of $-2\delta_2'$. Except for the rough allowance for finite span included in the interference parameters of Table 3, the method of interference correction proceeds as if the wing were of negligible span.

3.3. Correction to Pitching Derivatives

The present study requires two types of wall-interference correction. In the cases when the perforated screens are sealed ($1/P_E = \infty$) or completely removed ($1/P_E = 0$), equations (28) and the analysis in Ref. 1 hold good. With the effects of slot parameter F and span ratio σ included in the interference parameters, certain terms in the analysis are omitted and the practical procedure in equations (58) of Ref. 1 is followed. The tunnel values of the pitching derivatives $l_{\theta T}$, $m_{\theta T}$, $l_{\dot\theta T}$ and $m_{\dot\theta T}$ are taken from uncorrected experiment, the rotary derivatives l_q and m_q are taken from theory, and the equations are solved for corrected experimental derivatives l_θ, m_θ, $l_{\dot\theta}$ and $m_{\dot\theta}$. The other type of correction, which will now be

developed, is to take l_θ, m_θ, $l_{\dot\theta}$ and $m_{\dot\theta}$ from theory and to calculate $l_{\theta T}$, $m_{\theta T}$, $l_{\dot\theta T}$ and $m_{\dot\theta T}$ for arbitrary $1/P_E$. The starting point is equation (27) associated with a streamwise distribution of lift $L(x)$ per unit length.

In place of equation (38) of Ref. 1, we now have

$$\frac{\bar{w}_i(x)}{U} = \int_0^l \frac{2L(\xi)}{\rho U^2 C}\left[\left\{1 + \frac{i\omega M^2(x-\xi)}{\beta^2 U}\right\}\left\{\delta_0 + \delta_1\frac{x-\xi}{\beta h} + \delta_2\left(\frac{x-\xi}{\beta h}\right)^2\right\}\right.$$
$$\left. + \frac{i\omega h}{\beta U}\left\{\delta_0' + \delta_1'\frac{x-\xi}{\beta h} + \delta_2'\left(\frac{x-\xi}{\beta h}\right)^2\right\}\right] d\xi, \tag{42}$$

where $0 < \xi < l$ denotes the streamwise extent of the wing. Then, as in Ref. 1, we write

$$\left.\begin{aligned} \int_0^l L(\xi)\,d\xi &= \tfrac{1}{2}\rho U^2 S(C_{LR} + i\bar{\nu}C_{LI}),\\ -\int_0^l L(\xi)\xi\,d\xi &= \tfrac{1}{2}\rho U^2 S\bar{c}(C_{mR} + i\bar{\nu}C_{mI}) \end{aligned}\right\} \tag{43}$$

and

$$-\int_0^l L(\xi)\xi^2\,d\xi = \tfrac{1}{2}\rho U^2 S\bar{c}^2(C_{mR}^* + i\bar{\nu}C_{mI}^*),$$

where the geometric mean chord $\bar{c} = S/(2s)$ and the frequency parameter $\bar{\nu} = \omega\bar{c}/U$. By equations (42) and (43)

$$\frac{\bar{w}_i(x)}{U} = \left[a_0 + a_1\frac{x}{\bar{c}} + a_2\left(\frac{x}{\bar{c}}\right)^2\right] + i\bar{\nu}\left[b_0 + b_1\frac{x}{\bar{c}} + b_2\left(\frac{x}{\bar{c}}\right)^2\right] + O(\bar{\nu}^2), \tag{44}$$

where

$$\left.\begin{aligned} a_0 &= \frac{S}{C}\left[\delta_0 C_{LR} + \frac{\delta_1\bar{c}}{\beta h}C_{mR} - \frac{\delta_2\bar{c}^2}{\beta^2 h^2}C_{mR}^*\right],\\ a_1 &= \frac{S}{C}\left[\frac{\delta_1\bar{c}}{\beta h}C_{LR} + \frac{2\delta_2\bar{c}^2}{\beta^2 h^2}C_{mR}\right],\\ a_2 &= \frac{S}{C}\left[\frac{\delta_2\bar{c}^2}{\beta^2 h^2}C_{LR}\right],\\ b_0 &= \frac{S}{C}\left[\frac{\delta_0' h}{\beta\bar{c}}C_{LR} + \frac{\delta_1' + M^2\delta_0}{\beta^2}C_{mR} - \frac{(\delta_2' + M^2\delta_1)\bar{c}}{\beta^3 h}C_{mR}^* + \delta_0 C_{LI} + \frac{\delta_1\bar{c}}{\beta h}C_{mI}\right],\\ b_1 &= \frac{S}{C}\left[\frac{\delta_1' + M^2\delta_0}{\beta^2}C_{LR} + \frac{2(\delta_2' + M^2\delta_1)\bar{c}}{\beta^3 h}C_{mR} + \frac{\delta_1\bar{c}}{\beta h}C_{LI}\right] \end{aligned}\right\} \tag{45}$$

and

$$b_2 = \frac{S}{C}\left[\frac{(\delta_2' + M^2\delta_1)\bar{c}}{\beta^3 h}C_{LR}\right].$$

In order to convert the complex interference upwash into an increment in aerodynamic loading, we shall use the subsonic low-frequency lifting-surface theory of Ref. 11. Following equation (5) of Ref. 11, we obtain

$$\frac{\bar{w}_i}{U}\left\{1 - \frac{i\omega M^2 x}{\beta^2 U}\right\} = (a_0\alpha_1 + a_1\alpha_2 + a_2\alpha_4) + i\bar{\nu}\left[(b_0\alpha_1 + b_1\alpha_2 + b_2\alpha_4) - \frac{M^2}{\beta^2}(a_0\alpha_2 + a_1\alpha_4 + a_2\alpha_6)\right], \tag{46}$$

where $\alpha_1 = 1$, $\alpha_2 = x/\bar{c}$, $\alpha_4 = (x/\bar{c})^2$ and $\alpha_6 = (x/\bar{c})^3$. Then by equations (4), (24) and (25) of Ref. 11, the load distribution corresponding to $\bar{w}_i/U$ is

$$\frac{\Delta\bar{p}_i}{\frac{1}{2}\rho U^2} = (a_0 l_1 + a_1 l_2 + a_2 l_4) + i\bar{\nu}\left[(b_0 l_1 + b_1 l_2 + b_2 l_4) + \frac{M^2 x}{\beta^2 \bar{c}}(a_0 l_1 + a_1 l_2 + a_2 l_4) + \frac{1}{\beta^2}(a_0 l_3 + a_1 l_5 + a_2 l_7) - \frac{M^2}{\beta^2}(a_0 l_2 + a_1 l_4 + a_2 l_6)\right], \tag{47}$$

where l_j is the steady loading coefficient corresponding to the incidence α_j, and respectively α_3, α_5 and α_7 are related to l_1, l_2 and l_4 by equation (23) of Ref. 11. When terms of order $(\bar{\nu}S/C)(\bar{c}/\beta h)^2$ are neglected, the coefficient a_2 disappears from the imaginary part of equation (47). In terms of the coefficients I_{Lj} and $I^*_{Lj} = -I_{mj}$ in equations (33) of Ref. 11, which may be regarded as known, we can integrate $\Delta\bar{p}_i$ over the planform to give real and imaginary parts of the incremental lift coefficient

$$\left.\begin{aligned} \delta C_{LR} &= \frac{1}{\beta}(a_0 I_{L1} + a_1 I_{L2} + a_2 I_{L4}) \\ \text{and} \\ \delta C_{LI} &= \frac{1}{\beta}\left[(b_0 I_{L1} + b_1 I_{L2} + b_2 I_{L4}) + \frac{M^2}{\beta^2}(a_0 I^*_{L1} + a_1 I^*_{L2}) + \frac{1}{\beta^2}(a_0 I_{L3} + a_1 I_{L5}) - \frac{M^2}{\beta^2}(a_0 I_{L2} + a_1 I_{L4})\right] \end{aligned}\right\}. \tag{48}$$

These increments are defined similarly to C_{LR} and C_{LI} in equations (43), and there are corresponding formulae

$$\left.\begin{aligned} \delta C_{mR} &= \frac{1}{\beta}(a_0 I_{m1} + a_1 I_{m2} + a_2 I_{m4}), \\ \delta C_{mI} &= \frac{1}{\beta}\left[(b_0 I_{m1} + b_1 I_{m2} + b_2 I_{m4}) + \frac{M^2}{\beta^2}(a_0 I^*_{m1} + a_1 I^*_{m2}) + \frac{1}{\beta^2}(a_0 I_{m3} + a_1 I_{m5}) - \frac{M^2}{\beta^2}(a_0 I_{m2} + a_1 I_{m4})\right] \\ \text{and} \\ \delta C^*_{mR} &= \frac{1}{\beta}(a_0 I^*_{m1} + a_1 I^*_{m2} + a_2 I^*_{m4}) \end{aligned}\right\} \tag{49}$$

for the increments to the other force coefficients occurring in equations (45). An iterative procedure can now be established. Given initial free stream theoretical values of the five quantities C_{LR}, C_{LI}, C_{mR}, C_{mI} and C^*_{mR}, we calculate the coefficients a_0, a_1, a_2, b_0, b_1 and b_2 from equations (45) and then the increments $\delta C_{LR}, \delta C_{LI}, \delta C_{mR}, \delta C_{mI}$ and δC^*_{mR} from equations (48) and (49). The quantities $(C_{LR} + \delta C_{LR}), (C_{LI} + \delta C_{LI})$, etc., are first approximations to the theoretical windtunnel values to be substituted in equations (45). Successive approximations to $\delta C_{LR}, \delta C_{LI}$, etc., can be obtained by repeating the process until convergence is achieved.

The procedure just described applies to arbitrary wing motion. The simplification in the case of pitching motion is that the coefficients I_{Lj}, I_{mj} and I^*_{mj} occurring in equations (48) and (49) also determine the free-stream aerodynamic forces. Initially, with unit amplitude of pitching oscillation

$$\left.\begin{aligned} C_{LR} &= 2l_\theta, \qquad C_{LI} = 2l_{\dot\theta} \\ C_{mR} &= 2m_\theta, \qquad C_{mI} = 2m_{\dot\theta} \end{aligned}\right\}, \tag{50}$$

and

where by equations (39) of Ref. 11 with pitching axis $x = x_0$

$$\left.\begin{aligned} l_\theta &= \frac{1}{2\beta} I_{L1}, \\ m_\theta &= \frac{1}{2\beta}\left[I_{m1} + \frac{x_0}{\bar c} I_{L1} \right], \\ l_{\dot\theta} &= \frac{1}{2\beta}\left[\frac{\beta^2 - M^2}{\beta^2} I_{L2} + \frac{1}{\beta^2} I_{L3} - \frac{M^2}{\beta^2} I_{m1} - \frac{x_0}{\bar c} I_{L1} \right] \end{aligned}\right\} \tag{51}$$

and

$$\left.\begin{aligned} m_{\dot\theta} = \frac{1}{2\beta}\Bigg[&\frac{\beta^2 - M^2}{\beta^2} I_{m2} + \frac{1}{\beta^2} I_{m3} + \frac{M^2}{\beta^2} I^*_{m1} \\ &+ \frac{x_0}{\bar c}\left\{ \frac{\beta^2 - M^2}{\beta^2} I_{L2} + \frac{1}{\beta^2} I_{L3} - \frac{1}{\beta^2} I_{m1} \right\} - \left(\frac{x_0}{\bar c}\right)^2 I_{L1} \Bigg]. \end{aligned}\right\}$$

Finally, after the iterative procedure has converged,

$$\left.\begin{aligned} l_{\theta T} &= \tfrac{1}{2}(C_{LR} + \delta C_{LR}), \qquad l_{\dot\theta T} = \tfrac{1}{2}(C_{LI} + \delta C_{LI}), \\ m_{\theta \tilde T} &= \tfrac{1}{2}(C_{mR} + \delta C_{mR}), \qquad m_{\dot\theta T} = \tfrac{1}{2}(C_{mI} + \delta C_{mI}) \end{aligned}\right\}. \tag{52}$$

and

The rotary derivatives required in the first type of interference correction are defined in equations (53) of Ref. 1

$$\left.\begin{aligned} l_q &= \frac{1}{2\beta}\left[I_{L2} - \frac{x_0}{\bar c} I_{L1} \right] \\ m_q &= \frac{1}{2\beta}\left[I_{m2} + \frac{x_0}{\bar c}(I_{L2} - I_{m1}) - \left(\frac{x_0}{\bar c}\right)^2 I_{L1} \right] \end{aligned}\right\}. \tag{53}$$

and

With these quantities substituted in equations (58) of Ref. 1, the appropriate sets of measured pitching derivatives ($1/P_E = 0$ or ∞) can be corrected to free-stream conditions. When P_E is finite and non-zero,

equations (45), (48) and (49) can be used to correct measured derivatives. The theoretical free-stream derivatives in equations (50) are replaced by experimental tunnel values. It is necessary to simulate a measurement of the real part of the second aerodynamic moment C^*_{mR} from equation (43) and also to devise semi-empirical coefficients I_{Lj}, I_{mj} and I^*_{mj} in place of the theoretical values. With such artifice equations (45) lead to the final values of a_0, a_1, a_2, b_0, b_1 and b_2, and without iteration δC_{LR}, δC_{LI}, etc., can be calculated. The corrected experimental values are then

$$\left.\begin{aligned} l_\theta &= l_{\theta T} - \tfrac{1}{2}\delta C_{LR}, & l_{\dot\theta} &= l_{\dot\theta T} - \tfrac{1}{2}\delta C_{LI} \\ \text{and} \quad m_\theta &= m_{\theta T} - \tfrac{1}{2}\delta C_{mR}, & m_{\dot\theta} &= m_{\dot\theta T} - \tfrac{1}{2}\delta C_{mI} \end{aligned}\right\}. \tag{54}$$

Provided that the empirical stages can be handled satisfactorily, the same procedure can be recommended in place of the simpler and more approximate one to be used in the limiting cases of sealed and ideal slots.

4. Numerical Results and Comparison with Experiment

The preceding methods are applied to the two planforms considered in Ref. 4. As defined in Fig. 6, the origin is taken at the root leading edge, the dimensions are referred to the geometric mean chord $\bar{c}$, the cropped delta and unswept tapered wings have respective aspect ratios $A = 2s/\bar{c} = 2{\cdot}64$ and 4·33. The unswept tapered wing has fore and aft pitching axes $x = x_0 = 0{\cdot}25c_r$ and $0{\cdot}75c_r$; those at rather similar positions on the cropped delta wing are also defined in Fig. 6.

The basic theoretical lifting-surface calculations have been carried out on the cropped delta and unswept tapered wings at $M = 0$, 0·6 and 0·8 by the method of Ref. 11 with $m = 23$ spanwise and $N = 3$ chordwise collocation stations and with spanwise integration parameter $q = 4$. The aerodynamic coefficients required in equations (48) and (49) are calculated from equations (33) of Ref. 11 and listed in Table 4, and from equations (51) and (53) the necessary pitching derivatives of the respective wings are given for both axes in Tables 5a and 7a. From these free-stream values of l_θ, $l_{\dot\theta}$, m_θ and $m_{\dot\theta}$, the corresponding theoretical windtunnel values have been calculated with the two extreme and three intermediate porosity conditions for which the interference parameters are given in Table 3 (Section 3.2). Equations (50), (45), (48) with $I^*_{Lj} = -I_{mj}$, (49) and after iteration equation (52) are used to obtain these results for the three Mach numbers and both pitching axes in Tables 5b and 7b for the cropped delta and unswept tapered wings respectively.

The experimental data for the cropped delta half-model have been smoothed against Mach number and are available for round values including $M = 0{\cdot}6$ and 0·8. Some of the data are tabulated in Table 5 of Ref. 3 and, excluding those without perforated screens ($1/P_E = 0$), all are plotted in Figs. 6a to 9c of Ref. 4. It is sufficient here to list the smoothed uncorrected data in Table 6a over the range $0{\cdot}40 \leqslant M \leqslant 0{\cdot}85$ for the extremes of porosity. For the unswept tapered wing on the other hand, the experimental derivatives are unsmoothed and all the available uncorrected data in the range $0{\cdot}405 \leqslant M \leqslant 0{\cdot}886$ are given in Table 8. The corrections to free-stream conditions have been made for both wings by the approximate practical procedure in equations (58) of Ref. 1 where it is applicable ($1/P_E = 0$ and ∞). The required theoretical values of l_q and m_q from Tables 5a and 7a have been interpolated in M and used in the calculation of corrected experimental derivatives in Tables 6b and 9 respectively.

These numerical results from theory and experiment are analysed separately and then correlated for the cropped delta wing in Section 4.1 and for the unswept tapered wing in Section 4.2.

4.1. Cropped Delta Wing

As the two half-models are of the same span ratio $\sigma = 0{\cdot}385$, the smaller aspect ratio of the cropped delta wing gives the higher area ratio $S/C = 0{\cdot}1428$ and larger chord to height ratio $\bar{c}/h = 0{\cdot}3751$. The theoretical interference calculations in Table 5b neglect certain terms of order $(\bar{v}S/C)(\bar{c}/\beta h)^2$ included in equation (47); although this approximation may be acceptable, that used in Table 6b ignores terms of

lower order $(\bar{v}S/C)(\bar{c}/\beta h)$, as can be seen from equations (56) and (57) of Ref. 1. The uncertainty due to this latter approximation proves not to be too important, because the investigation of Ref. 3 has provided an independent interference-free datum from experiments on the same half-model in three larger tunnels.

The calculated derivatives of pitching moment in Table 5b for the aft axis are plotted against Ψ from equation (23); Fig. 7 gives a curve for each Mach number, and in each case the free-stream value from Table 5a is plotted as a circle on the curve, to indicate the value of the porosity parameter Ψ for which there is no theoretical effect of wall interference. The limited range $0{\cdot}40 < \Psi < 0{\cdot}48$ suggests that the interference-free condition for both stiffness and damping derivatives is not very sensitive to changes in Mach number.

The experimental results for the aft axis from Tables 6a and 6b are all plotted against Mach number in Figs. 8 and 9. Although the corrected values of each derivative for the extreme roof and floor conditions are much closer together than the corresponding uncorrected curves, the lift derivatives l_θ and $l_{\dot{\theta}}$ are less satisfactory than m_θ and $m_{\dot{\theta}}$. The full curves are drawn to represent mean corrected experimental data between the two sets of crosses, which are assumed to be equally inaccurate as a consequence of the approximations discussed above. It is remarkable how well these mean curves agree with those labelled 'interference-free datum' in Figs. 8a, 8c, 8e and 8g of Ref. 3. Moreover, with the exception of $l_{\dot{\theta}}$, the mean curves against M have shapes similar to the theoretical curves of long and short dashes in Figs. 8 and 9. Also for the aft axis, the uncorrected experimental derivatives $m_{\theta T}$, $m_{\dot{\theta} T}$ and $l_{\dot{\theta} T}$ from Table 6a or from Refs. 3 and 4 are plotted in Fig. 10 against Ψ as calibrated for the different hole sizes in Fig. 2. The curves are drawn for $M = 0{\cdot}6$ and $0{\cdot}8$, and in each case both corrected values from Table 6b (except the smaller value of $l_{\dot{\theta}}$ for $M = 0{\cdot}8$) are plotted on the curves, as was done for the theoretical data in Fig. 7. The average values of Ψ for zero interference on $m_{\theta T}$ are still in the range $0{\cdot}40 < \Psi < 0{\cdot}48$, but the damping derivatives seem to require smaller values nearer 0·25.

In the final analysis in Figs. 11 and 12, it is best to consider the derivatives of pitching moment about two axes, because the experimental lift derivatives are merely deduced from measurements of pitching moment (Section 5 of Ref. 4). Having established a reasonably consistent behaviour of wall interference at different Mach numbers, we take $M = 0{\cdot}8$ for which the effects are greatest. The theoretical and uncorrected experimental curves of $m_{\theta T}$ and $m_{\dot{\theta} T}$ against Ψ are plotted. The theoretical free-stream values again appear as circles on the curves, while the 'interference-free datum' from Ref. 3 is plotted at $\Psi = 0{\cdot}355$ corresponding to the perforated screens with 0·06 in (1·6 mm) holes. There are encouraging similarities in the trends of wall effects as calculated and observed, even as regards the minimum in the damping about the fore axis in Fig. 11 near $\Psi = 0{\cdot}4$. The theoretical interference-free condition clearly depends on axis position and seems to require a larger value of Ψ than 0·355, which minimizes experimental interference. The points (λ) from experiments in the original NPL $9\frac{1}{2}$ in × $9\frac{1}{2}$ in (24 cm × 24 cm) slotted tunnel (Figs. 8a to 9c of Ref. 4) show how the investigation of wall interference has reduced uncertainties by an order of magnitude.

4.2. Unswept Tapered Wing

The higher aspect ratio of the unswept tapered wing makes it more susceptible to tunnel interference despite its lower area ratio $S/C = 0{\cdot}0862$ and chord to height ratio $\bar{c}/h = 0{\cdot}2276$. The wall corrections can be expected to be larger and more accurate. The presentation of results in Figs. 13 to 18 follows a similar pattern to that described in detail for the cropped delta wing.

Thus Fig. 13 shows a small effect of Mach number on the theoretical interference-free wall condition, and the tendency for the optimum Ψ to increase with M is slightly greater than in Fig. 7 for the cropped delta wing. It is fortunate, therefore, that in Fig. 2 a similar increase in the calibrated Ψ is found for fixed wall geometry as M changes from 0·6 to 0·8. Smaller values of Ψ are required for damping than for stiffness, but the inclusive range $0{\cdot}35 < \Psi < 0{\cdot}50$ covers both wings. Figs. 14 and 15 are equally satisfactory for pitching moment and lift. The mean corrected experimental curves of l_θ and $l_{\dot{\theta}}$ against Mach number for the aft axis carry some conviction, unlike those in Figs. 8 and 9. We can have sufficient confidence in the practical interference correction of Ref. 1 to use the mean curves in place of an independent experimental interference-free datum for the unswept tapered wing.

The uncorrected experimental data in Table 8 only include two hole sizes of the perforated screen, so that the curves in Fig. 16 are less well defined than those in Fig. 10. The Mach numbers $M = 0{\cdot}608$ and $0{\cdot}812$ require interpolation in a few cases. The pairs of circles on the curves correspond to the sets of corrected data shown as crosses in Figs. 14 and 15, and again they denote values of Ψ for which particular measured derivatives, $m_{\theta T}$, $m_{\dot{\theta} T}$ and $l_{\dot{\theta} T}$, become free of interference. In each case the trend in optimum Ψ with increasing M is different for slots sealed and for slots open, but the theoretical trend in Fig. 13 is reversed, if anything. The experimental condition $\Psi = 0{\cdot}45$ is selected to minimize interference.

The synthesis of theoretical and experimental effects of wall porosity is accomplished in Figs. 17 and 18. The free-stream theoretical values for $M = 0{\cdot}8$ appear as circles on the curves, while mean corrected experimental values for $M = 0{\cdot}812$ from Table 9 or Figs. 14 and 15 are plotted as triangles at the selected position $\Psi = 0{\cdot}45$. The practical success is measured by the closeness of the triangles to the dashed curves; the discrepancies are of the order ± 3 per cent, except for $-l_{\dot{\theta}}$ which is 6 per cent too high. These encouraging results could even be improved by choosing $\Psi = 0{\cdot}60$ for the stiffness derivatives in Fig. 17 and $\Psi = 0{\cdot}40$ for the damping derivatives in Fig. 18. The theoretical success is judged by the qualitative similarity between the full and dashed curves and by comparison of the predicted interference-free conditions. The curves are remarkably similar throughout and, indeed, $\Psi = 0{\cdot}60$ serves quite well theoretically in Fig. 17, while $\Psi = 0{\cdot}40$ is not far wide of the mark in Fig. 18.

Because the frequency parameter is small ($\bar{\nu} < 0{\cdot}15$), it is possible to estimate the pitching damping as a function of axis position

$$m_{\dot{\theta}} = m_{\dot{\theta}1} + \frac{x_0 - x_1}{\bar{c}}(l_{\dot{\theta}1} - m_{\theta 1}) - \left(\frac{x_0 - x_1}{\bar{c}}\right)^2 l_{\theta 1}, \tag{55}$$

given the set of derivatives $l_{\theta 1}$, $l_{\dot{\theta}1}$, $m_{\theta 1}$, $m_{\dot{\theta}1}$ for a particular pitching axis $x = x_1$. In Fig. 19, parabolic curves of $-m_{\dot{\theta}}$ have been drawn from the uncorrected experimental data with slots open, with slots sealed and interpolated to correspond to the optimum wall conditions $\Psi = 0{\cdot}355$ for the cropped delta wing and $\Psi = 0{\cdot}45$ for the unswept tapered wing. The free-stream theoretical curves of large and small dashes are included for comparison, and for both wings the resemblance in shape between these and the interpolated full curves gives added confidence that the major effects of wall interference have been removed.

5. Recommended Practical Procedure

Section 6.1 of Ref. 4 describes a general method of modifying ventilated walls to minimize interference on dynamic measurements. The suggestions, by Moore and Wight, are paraphrased as follows:

(a) Choose a model, such as the unswept tapered wing, that is amenable to theoretical treatment, sensitive to wall interference and preferably of area ratio $S/C < 0{\cdot}1$.

(b) Seal the ventilated walls and measure pitching moment derivatives $m_{\theta T}$ and $m_{\dot{\theta} T}$ at $M = 0{\cdot}8$ about a pitching axis well aft of the aerodynamic centre.

(c) Estimate values of $l_{\theta T}$, $l_{\dot{\theta} T}$, l_q and m_q, and then correct the measured derivatives for wall interference by equations (58) of Ref. 1 with interference parameters $\delta_0^{(1)}$, $\delta_1^{(1)}$ and $\delta_0'^{(1)}$ modified in the ratio $(\delta_0^{(1)})_E/\delta_0^{(1)}$.

(d) Determine by experiment suitable perforated screens which, when fitted behind the ventilated walls, give the corrected value of $m_{\dot{\theta}}$.

They also suggest that, when there are perforated liners, there is greater danger that the wall condition for interference-free measurements may be dependent on Mach number; in any case, it is advisable to include a lower Mach number $M = 0{\cdot}6$ in (b). Since the interference corrections are more dependent on lift than on pitching moment or centre of lift a second pitching axis is also advantageous, because $l_{\theta T}$ and $l_{\dot{\theta} T}$ are then better defined; moreover, the derivative $l_{\dot{\theta} T}$ is especially sensitive to wall interference and may provide a better criterion than $m_{\dot{\theta} T}$. The larger the model, the greater the uncertainty in (c). The corrections to damping derivatives, though smaller for closed than for ideal slotted roof and floor, are not necessarily more accurate. Indeed, the present analysis is based on the mean corrected experimental curves in Figs. 8, 9, 14 and 15 giving equal weight to the results for slots closed and slots open. Thus,

in the case of walls with longitudinal slots wide enough to avoid viscous effects from the tunnel boundary layer, say, with $a > 0{\cdot}02b$, there is a case for repeating (b) and (c) with slots open and no perforated screen. In (d) it is advisable to optimize the wall conditions for both $l_{\dot{\theta}}$ and $m_{\dot{\theta}}$ corresponding to the aft pitching axis.

There is a clear indication from theory and experiment that the porosity parameter Ψ to minimize interference on stiffness derivatives exceeds the optimum for $l_{\dot{\theta}}$ and $m_{\dot{\theta}}$ with aft pitching axis. A glance at equation (55) is sufficient warning that the optimum Ψ for interference-free damping derivatives may change with axis position. It is also necessary to deal with a practical situation without calibrated data, such as in Fig. 2, when it is not possible to estimate what value of P_E to use in theoretical calculations. The following procedure is then recommended as a further extension to that of Ref. 4:

(i) Calculate interference parameters by the method of Ref. 7 for the known slot geometry, but variable $1/P_E$, and allow for numerical errors and model span as described in Sections 3.1 and 3.2.

(ii) With the aft experimental pitching axis $x = x_1$, say, apply the theoretical method of Section 3.3 at $M = 0{\cdot}8$ to discover the value of $1/P_E$ for which $l_{\dot{\theta}1}$ and $m_{\dot{\theta}1}$ are approximately interference-free.

(iii) For this value of $1/P_E$, calculate the theoretical quantities $l_{\theta T}$ and $m_{\theta T}$ for the axis $x = x_1$, and hence the incremental corrections $(l_\theta - l_{\theta T})$ and $(m_\theta - m_{\theta T})$; modify these in the ratio of the uncorrected experimental $l_{\theta T}$ to its theoretical value, and then add them to the measured derivatives to give $l_{\theta 1}$ and $m_{\theta 1}$.

(iv) Convert the derivatives to arbitrary pitching axis by means of equation (55) and the simpler relations

$$\left.\begin{aligned} m_\theta &= m_{\theta 1} + \frac{x_0 - x_1}{\bar{c}} l_{\theta 1} \\ \text{and} \qquad l_{\dot{\theta}} &= l_{\dot{\theta}1} - \frac{x_0 - x_1}{\bar{c}} l_{\theta 1} \end{aligned}\right\}. \tag{56}$$

This sequence of calculations will first be made for the unswept tapered wing, and application to the cropped delta wing will then be simulated.

It is supposed that the pitching moments have been measured on the unswept tapered wing at $M = 0{\cdot}812$ for two pitching axes and with slots both sealed and open. At stage (d) the roof and floor of the $9\frac{1}{2}$ in $\times$ $9\frac{1}{2}$ in (24 cm $\times$ 24 cm) tunnel are optimized by choosing an experimental porosity condition $\Psi = 0{\cdot}40$ to equate the measured and corrected experimental damping derivatives in Fig. 18 as well as possible. Operation (i) of the extended procedure is covered in Tables 2 and 3. Operation (ii) comprises the calculations in Tables 4 and 7 for the unswept tapered wing at $M = 0{\cdot}8$ and the circles on the top and bottom full curves in Fig. 18, which give a mean theoretical condition $\Psi = 0{\cdot}44$. Operation (iii) is carried out with interpolated quantities at $M = 0{\cdot}812$ and $\Psi = 0{\cdot}44$ to correct the measured stiffness derivatives for $x_0 = 1{\cdot}185\bar{c}$ corresponding to $\Psi = 0{\cdot}40$. The corrected values are obtained as

$$l_{\theta 1} = (l_{\theta T})_{\text{meas.}} + \frac{(l_{\theta T})_{\text{meas.}}}{(l_{\theta T})_{\text{theory}}} (l_\theta - l_{\theta T})_{\text{theory}} \tag{57}$$

$$= 2{\cdot}34 + 0{\cdot}92(2{\cdot}50\text{–}2{\cdot}55) = 2{\cdot}29.$$

Similarly

$$m_{\theta 1} = 1{\cdot}56 + 0{\cdot}92(1{\cdot}72\text{–}1{\cdot}74) = 1{\cdot}54.$$

Both these values are in satisfactory agreement with the interference-free points ($l_\theta = 2{\cdot}27$, $m_\theta = 1{\cdot}52$) in Fig. 17.

The final check is to use the same porosity conditions $\Psi = 0{\cdot}44$ theoretically and $\Psi = 0{\cdot}40$ from experiment, so as to deduce corrected experimental data for the cropped delta wing. For the pitching

axis $x_0 = 1{\cdot}039\bar{c}$ and $M = 0{\cdot}6$ and $0{\cdot}8$, we have the following tabulated derivatives from Fig. 10 and from similar interpolation in the measured values of $l_{\theta T}$.

Experiment $\Psi = 0{\cdot}40$	$M = 0{\cdot}6$	$M = 0{\cdot}8$
$l_{\theta T}$	1·58	1·71
$l_{\dot{\theta} T}$	0·46	0·31
$m_{\theta T}$	0·59	0·63
$-m_{\dot{\theta} T}$	0·19	0·36

Corresponding to equation (57) and with data from Tables 5a and 5b ($\Psi = 0{\cdot}44$), there are corrected stiffness derivatives

$$\left.\begin{aligned} l_{\theta 1} &= 1{\cdot}58 + 0{\cdot}96(1{\cdot}60 - 1{\cdot}65) = 1{\cdot}53 \quad \text{for } M = 0{\cdot}6 \\ &= 1{\cdot}71 + 0{\cdot}93(1{\cdot}74 - 1{\cdot}84) = 1{\cdot}62 \quad \text{for } M = 0{\cdot}8 \end{aligned}\right\}$$

and the theoretical corrections to $m_{\theta T}$ are negligible. No corrections are applied to $l_{\dot{\theta} T}$ and $-m_{\dot{\theta} T}$. In Table 10, these results are compared with the two independent estimates of interference-free experimental derivatives. Firstly, we use the mean corrected experimental curves from Figs. 8 and 9, which incorporate equations (58) of Ref. 1 : secondly, the 'interference-free datum' values, deduced from the previous experiments in the three relatively large ventilated tunnels, are read from Figs. 8a, 8c, 8e and 8g of Ref. 3. Only in case of $l_{\dot{\theta}}$ do the discrepancies exceed 4 per cent of l_{θ}, probably because the uncorrected values of $l_{\dot{\theta}}$ are notoriously difficult to determine experimentally. Provided that the span ratio $\sigma < 0{\cdot}4$ and the area ratio $S/C < 0{\cdot}15$, it is realistic to conclude that, with sufficient care, the uncertainties of ventilated wall interference on dynamic experiments with moderately small frequency parameter can be reduced to the order of 5 per cent of the in-phase lift derivative, e.g., $0{\cdot}05 l_{\theta}$. Models of larger span or area ratio should be avoided, unless the required accuracy is relatively low.

6. Conclusions

(1) The theory of Ref. 1 for small frequency is now extended to subsonic rectangular tunnels with a more general homogeneous boundary condition representing a ventilated roof and floor with longitudinal slots and perforated screens of arbitrary porosity.

(2) Instead of the usual three, there are six interference parameters to calculate; all, except perhaps δ_0, are found to be highly non-linear functions of the porosity parameter Ψ.

(3) On the basis of steady flow with elliptic spanwise loading, a simple analytical formula for $(\delta_0)_E$ has been derived in Section 3.2. The ratio $(\delta_0)_E/\delta_0$ shows important effects of span ratio σ, which are magnified by the large breadth to height ratio of the effective tunnel ($b/h = 2{\cdot}6$).

(4) Given Ψ, the theoretical wind-tunnel conditions can be calculated by an iterative procedure. To minimize wall interference on pitching damping derivatives in the $9\frac{1}{2}$ in $\times$ $9\frac{1}{2}$ in (24 cm $\times$ 24 cm) slotted tunnel, the optimum porosity parameter is $\Psi = 0{\cdot}44$ in remarkably close agreement with the value $\Psi = 0{\cdot}40$ indicated by experiment.

(5) Theory and experiment combine to show that the optimum ventilated wall is hardly influenced by Mach number, so that there are good prospects of eliminating the major interference effects at transonic speeds.

(6) Each pitching derivative, when plotted against porosity parameter, shows qualitatively similar behaviour theoretically and experimentally. While the best choice of Ψ is not greatly dependent on planform, there is a consistent tendency for stiffness derivatives to require larger values corresponding to more open perforated screens.

(7) The practical procedure of Ref. 4 for choosing a suitable ventilated wall is extended to indicate how, after the interference on damping derivatives with aft pitching axis has been minimized, residual corrections to stiffness derivatives can be calculated, and hence residual corrections to damping derivatives with arbitrary axis (Section 5).

(8) With sufficient care, the uncertainties of ventilated wall interference on dynamic measurements with moderately small frequency parameter and subsonic Mach number can probably be reduced to the order of 5 per cent of the in-phase lift derivative, provided that the span ratio $\sigma < 0{\cdot}4$ and the area ratio $S/C < 0{\cdot}15$.

(9) At the end of Section 3.3 a possible direct evaluation of wall interference on measured pitching derivatives is indicated. Although this is as yet untried because of its empirical element, it represents an alternative approach when it is inconvenient to alter a wall of known porosity.

(10) The major limitations of the present theoretical analysis are the upper restrictions on frequency and model size, lack of information on the spanwise variation of the out-of-phase interference upwash, and the unsuitability of elliptic spanwise loading for elastic modes or part-span control surfaces. Some progress in these respects is anticipated from extensions to Ref. 7 and other current work.

Acknowledgements

The author acknowledges the assistance of Mrs. Sylvia Lucas with the extensive calculations and the preparation of diagrams, and also some helpful discussions with his colleague Dr. A. W. Moore on the interpretation of experimental data. The investigation would not have been possible without the co-operation of Dr. K. R. Rushton and Mrs. Lucy Tomlinson (née Laing) of the Department of Civil Engineering at the University of Birmingham, who provided the vital approximate values of the interference parameters under contract to the Ministry of Technology.

LIST OF SYMBOLS

a	Width of slot
a_0, a_1, a_2	Coefficients in equations (44) and (45)
A	Aspect ratio of wing, $2s/\bar{c}$
b	Effective breadth of tunnel
b_0, b_1, b_2	Coefficients in equations (44) and (45)
c_r, c_t	Root chord, tip chord
$\bar{c}$	Geometric mean chord of wing, $S/2s$
C	Cross-sectional area of tunnel
C_L	Lift/qS, $\bar{C}_L e^{i\omega t}$
$\bar{C}_L$	Complex lift coefficient, $C_{LR} + i\bar{\nu}C_{LI}$
C_m	Pitching moment/$qS\bar{c}$, $\bar{C}_m e^{i\omega t}$
$\bar{C}_m$	Complex pitching moment coefficient, $C_{mR} + i\bar{\nu}C_{mI}$
C_m^*	Second pitching moment/$qS\bar{c}^2$ in equation (43)
d	Periodic spacing of slots (Fig. 1)
F	Non-dimensional slot parameter in equation (5)
g	Gap between half-model and side-wall
h	Height of tunnel
I_k	Coefficients in equations (32) and (33)
I_{Lj}	Equivalent C_L for incidence α_j
$I_{mj} = -I_{Lj}^*$	Equivalent C_m for incidence α_j } defined in equations (33) of Ref. 11
I_{mj}^*	Equivalent C_m^* for incidence α_j
J_1	Bessel function of the first kind
l	Streamwise extent of planform
l_j	Non-dimensional loading $\Delta p/q$ for incidence α_j
l_q, m_q	Rotary pitching derivatives in equations (53)
l_θ, m_θ	Pitching stiffness derivatives in equations (50) and (51)
$l_{\dot{\theta}}, m_{\dot{\theta}}$	Pitching damping derivatives in equations (50) and (51)
L	Lift per unit streamwise distance
m	Number of spanwise collocation sections
M	Mach number of undisturbed stream
n	Outward normal distance from tunnel boundary
N	Number of chordwise collocation points
Δp	Pressure difference between upper and lower surfaces
$\Delta\bar{p}_i$	Complex pressure difference due to wall interference

LIST OF SYMBOLS (Contd)

P	Porosity parameter in equation (4), βP_E
P_E	Measured porosity parameter in equation (9)
q	Dynamic pressure of undisturbed stream, $\frac{1}{2}\rho U^2$
q	Spanwise integration parameter in Ref. 11
s	Semi-span of wing
S	Area of planform of wing
t	Time
U	Velocity of undisturbed stream
v_n	Mean velocity normal to ventilated wall
w_i	Interference upwash velocity, $\bar{w}_i\, e^{i\omega t}$
$\bar{w}_i$	Complex interference upwash velocity
x	Streamwise distance downstream from root leading edge
x_0	Value of x at pitching axis
X	modified streamwise distance, x/β
y	Spanwise distance from wing root
z	Upward distance from centre of tunnel
α_j	Steady distributions of incidence in equations (46) and (47)
α_k	Function in equation (33)
β	Compressibility factor, $(1 - M^2)^{\frac{1}{2}}$
$\delta_0, \delta_1, \delta_2$	Steady upwash interference parameters in equation (25)
$\delta'_0, \delta'_1, \delta'_2$	Interference parameters in imaginary part of equation (25)
η	Non-dimensional spanwise distance, $2y/b$
Θ_k	Function in equation (38)
λ_1, λ_2	Approximate corrective factors below equation (40)
Λ_0	Angle of sweepback of leading edge
$\bar{\nu}$	Frequency parameter, $\omega\bar{c}/U$
ρ	Density of undisturbed stream
σ	Span ratio, $2s/b$
τ	Span of uniform loading as a fraction of b
ϕ	Perturbation velocity potential, $\bar{\phi}\, e^{i\omega t}$
$\bar{\phi}$	Complex perturbation velocity potential
$\bar{\phi}_i$	Complex potential due to wall interference
$\bar{\phi}_m$	Complex potential due to lifting model

LIST OF SYMBOLS (Contd)

ψ	Potential function in equation (12)
Ψ	Porosity parameter in equation (23)
ω	Angular frequency of oscillation
Ω	Modified frequency, ω/β
1	Subscript denoting pitching axis $x = x_1$
E	Subscript denoting elliptic spanwise loading
i	Subscript denoting effect of wall interference
I	Subscript denoting imaginary part in equations (43) or (29) and (30)
j	Subscript denoting incidence α_j
m	Subscript denoting model only
R	Subscript denoting real part
T	Subscript denoting derivative with tunnel-wall constraint
δ	Prefix denoting increment due to wall constraint
(1)	Superscript denoting closed tunnel
(4)	Superscript denoting closed side-walls, open roof and floor

REFERENCES

No.	*Author(s)*	*Title, etc.*
1	H. C. Garner, A. W. Moore and K. C. Wight ..	The theory of interference effects on dynamic measurements in slotted-wall tunnels at subsonic speeds and comparisons with experiment. ARC R & M 3500 (1966).
2	A. W. Moore and K. C. Wight	An experimental investigation of wall interference effects on dynamic measurements on half-models in ventilated tunnels through the transonic speed range. ARC R & M 3570 (1967).
3	A. W. Moore and K. C. Wight	On achieving interference-free results from dynamic tests on half-models in transonic wind tunnels. ARC R & M 3636 (1969).
4	A. W. Moore and K. C. Wight	An experimental investigation of wind-tunnel wall conditions for interference-free dynamic measurements. NPL Aero Report 1307 ARC 31704 (1969).
5	B. S. Baldwin, J. B. Turner and E. D. Knechtel ..	Wall interference in wind tunnels with slotted and porous boundaries at subsonic speeds. NACA Technical Note 3176 (1954).
6	K. R. Rushton and Lucy M. Laing	A digital computer solution of the Laplace equation using the dynamic relaxation method. Aeronaut. Q. Vol. XIX, pp. 375–387 (1968).
7	K. R. Rushton and Lucy M. Tomlinson	Theoretical solutions of oscillatory lift interference. Part I. ARC R & M 3700 (1971).
8	D. R. Holder	Upwash interference on wings of finite span in a rectangular wind tunnel with closed side walls and porous-slotted floor and roof. ARC R & M 3395 (1963).
9	E. W. E. Rogers	Wall interference in tunnels with ventilated walls. Subsonic Wind Tunnel Wall Corrections, Chapter VI. AGARDograph 109 (1966).
10	H. C. Garner	Lift interference on three-dimensional wings. Subsonic Wind Tunnel Wall Corrections, Chapter III. AGARDograph 109 (1966).
11	H. C. Garner and D. A. Fox	Algol 60 programme for Multhopp's low-frequency subsonic lifting-surface theory. ARC R & M 3517 (1966).

TABLE 1

Analytical Formulae for Interference Parameters for Rectangular Tunnels with Closed Side-Walls

Roof and floor	δ_0	δ_1	δ'_0	$(\delta_0)_E$
Closed	Ref. 1, eq. (20), $\delta_0^{(1)}$ and $\delta_0^{(4)}$	Ref. 1, eq. (22), $\delta_1^{(1)}$ and $\delta_1^{(4)}$	Ref. 1, eq. (28)	Ref. 10, eq. (3.84)
Open			Ref. 1, eqs. (36), (28), (30)	Ref. 1, eqs. (63) to (65)
Ideal slotted	Ref. 9, eq. (6.68)·	—	—	Eq. (38)
Slotted-perforated	Ref. 9, eq. (6.73)	—	—	Eq. (37)

TABLE 2

Interference Parameters for Small Wings in Rectangular Tunnel ($b/h = 2{\cdot}6$) with Closed Side-Walls and Variable Roof and Floor

Roof and floor		Exact	Approximate results (Ref. 7)					
F	$1/P_E$	δ_0	δ_0	δ_1	δ_2	δ'_0	δ'_1	δ'_2
any	∞	0·1713	0·191	0·444	0·000	−0·005	−0·191	−0·205
0·233	7·0		0·148	0·437	0·083	−0·003	−0·194	−0·211
0·233	3·0	0·0806	0·093	0·404	0·176	0·009	−0·188	−0·224
0·233	1·5		0·018	0·317	0·268	0·037	−0·152	−0·240
0·233	1·0	−0·0351	−0·033	0·232	0·293	0·062	−0·103	−0·228
0·233	0·4	−0·1276	—	—	—	—	—	—
0·233	0	−0·2216	−0·215	−0·233	0·000	0·165	0·215	0·118
0	0	−0·3403	−0·342	−0·507	0·000	0·205	0·342	0·247

TABLE 3

Interference Parameters Used in the Calculations ($b/h = 2{\cdot}6$, *Closed Side-Walls*, $\sigma = 0{\cdot}385$)

Roof and floor		δ_0	δ_1	δ_2	δ'_0	δ'_1	δ'_2
F	$1/P_E$						
0·233	∞	0·1237	0·2701	0	−0·0006	−0·1237	−0·1350
0·233	3·0	0·0486	0·2838	0·1760	0·0077	−0·1436	−0·1746
0·233	1·0	−0·0464	0·1852	0·2930	0·0529	−0·0896	−0·2065
0·233	0·4	−0·1209	0·0308	0·2265	0·1011	0·0263	−0·1010
0·233	0	−0·1950	−0·2077	0	0·1452	0·1950	0·1038

TABLE 4

Theoretical Aerodynamic Coefficients for Two Wings (*Method of Ref.* 11 *with* $m = 23$, $N = 3$, $q = 4$)

Coeff.	Cropped delta wing			Unswept tapered wing		
	$M = 0$	$M = 0{\cdot}6$	$M = 0{\cdot}8$	$M = 0$	$M = 0{\cdot}6$	$M = 0{\cdot}8$
I_{L1}	2·952	2·564	2·091	3·851	3·469	2·959
I_{L2}	3·571	3·131	2·592	4·153	3·755	3·224
I_{L3}	0·540	0·752	0·868	−0·356	0·161	0·618
I_{L4}	4·514	3·982	3·329	4·797	4·344	3·742
I_{L5}	0·220	0·504	0·692	−0·837	−0·267	0·252
$-I_{m1}$	1·875	1·624	1·320	1·940	1·734	1·459
$-I_{m2}$	2·697	2·393	2·014	2·568	2·342	2·036
$-I_{m3}$	0·677	0·799	0·849	0·266	0·513	0·717
$-I_{m4}$	3·735	3·354	2·872	3·305	3·040	2·679
$-I_{m5}$	0·509	0·676	0·773	0·010	0·286	0·524
$-I^*_{m1}$	1·465	1·260	1·012	1·294	1·145	0·947
$-I^*_{m2}$	2·391	2·131	1·807	2·010	1·840	1·608
$-I^*_{m4}$	3·545	3·212	2·787	2·820	2·615	2·330

TABLE 5

Calculated Theoretical Pitching Derivatives for Cropped Delta Wing

(a) *Free stream (Table 4)*

$x_0/\bar{c}$	M	l_θ	$l_{\dot{\theta}}$	m_θ	$-m_{\dot{\theta}}$	l_q	$-m_q$
0·314	0	1·476	1·592	−0·474	0·893	1·322	0·639
	0·6	1·602	1·659	−0·512	1·037	1·454	0·720
	0·8	1·743	1·738	−0·553	1·269	1·613	0·826
1·039	0	1·476	0·522	0·596	0·171	0·252	0·113
	0·6	1·602	0·497	0·649	0·306	0·292	0·137
	0·8	1·743	0·474	0·710	0·524	0·350	0·172

(b) *Slotted tunnel with variable porosity*

M	$1/P_E$	$l_{\theta T}$	$x_0 = 0{\cdot}314\bar{c}$			$x_0 = 1{\cdot}039\bar{c}$		
			$l_{\dot{\theta}T}$	$-m_{\theta T}$	$-m_{\dot{\theta}T}$	$l_{\dot{\theta}T}$	$m_{\theta T}$	$-m_{\dot{\theta}T}$
0	∞	1·598	1·649	0·523	0·919	0·490	0·635	0·184
	3·0	1·555	1·588	0·511	0·891	0·460	0·616	0·186
	1·0	1·484	1·598	0·486	0·887	0·522	0·590	0·156
	0·4	1·417	1·653	0·458	0·905	0·626	0·569	0·120
	0	1·340	1·707	0·424	0·926	0·735	0·548	0·085
0·6	∞	1·761	1·714	0·579	1·075	0·437	0·698	0·338
	3·0	1·715	1·620	0·569	1·023	0·377	0·675	0·338
	1·0	1·628	1·646	0·537	1·012	0·465	0·644	0·286
	0·4	1·540	1·751	0·498	1·046	0·635	0·618	0·225
	0	1·436	1·859	0·449	1·086	0·818	0·592	0·167
0·8	∞	1·961	1·801	0·652	1·348	0·380	0·770	0·600
	3·0	1·921	1·615	0·649	1·228	0·222	0·744	0·596
	1·0	1·813	1·642	0·608	1·180	0·328	0·706	0·501
	0·4	1·688	1·854	0·549	1·246	0·630	0·675	0·392
	0	1·532	2·076	0·468	1·329	0·965	0·643	0·290

TABLE 6

Smoothed Experimental Pitching Derivatives for Cropped Delta Wing

(a) *Uncorrected data*

Slots	M	$l_{\theta T}$	$x_0 = 0{\cdot}314\bar{c}$			$x_0 = 1{\cdot}039\bar{c}$		
			$l_{\dot{\theta} T}$	$-m_{\theta T}$	$-m_{\dot{\theta} T}$	$l_{\dot{\theta} T}$	$m_{\theta T}$	$-m_{\dot{\theta} T}$
Sealed $\frac{1}{P_E} = \infty$	0·40	1·574	1·603	0·555	0·875	0·462	0·586	0·138
	0·50	1·610	1·592	0·568	0·895	0·425	0·599	0·175
	0·60	1·657	1·577	0·587	0·923	0·376	0·614	0·225
	0·70	1·724	1·564	0·616	0·969	0·314	0·634	0·295
	0·80	1·818	1·531	0·656	1·055	0·213	0·662	0·425
	0·85	1·874	1·503	0·681	1·123	0·144	0·678	0·525
Open $\frac{1}{P_E} = 0$	0·40	1·324	1·773	0·450	0·960	0·813	0·510	0·044
	0·50	1·368	1·758	0·470	0·969	0·766	0·522	0·073
	0·60	1·423	1·755	0·494	0·991	0·723	0·538	0·109
	0·70	1·479	1·775	0·514	1·040	0·703	0·558	0·158
	0·80	1·531	1·823	0·530	1·131	0·713	0·580	0·230
	0·85	1·553	1·842	0·536	1·198	0·716	0·590	0·290

(b) *Corrected for wall interference* (Ref. 1)

Slots	M	l_θ	$x_0 = 0{\cdot}314\bar{c}$			$x_0 = 1{\cdot}039\bar{c}$		
			$l_{\dot{\theta}}$	$-m_\theta$	$-m_{\dot{\theta}}$	$l_{\dot{\theta}}$	m_θ	$-m_{\dot{\theta}}$
Sealed $\frac{1}{P_E} = \infty$	0·40	1·452	1·532	0·503	0·845	0·475	0·551	0·137
	0·50	1·480	1·523	0·512	0·864	0·446	0·563	0·171
	0·60	1·515	1·512	0·524	0·892	0·409	0·576	0·216
	0·70	1·564	1·504	0·543	0·937	0·364	0·593	0·280
	0·80	1.627	1·483	0·565	1·020	0·297	0·618	0·396
	0·85	1·659	1·467	0·575	1·087	0·256	0·632	0·485
Open $\frac{1}{P_E} = 0$	0·40	1·460	1·666	0·503	0·929	0·614	0·554	0·117
	0·50	1·515	1·616	0·528	0·926	0·522	0·568	0·161
	0·60	1·584	1·562	0·559	0·930	0·415	0·588	0·219
	0·70	1·659	1·511	0·588	0·956	0·309	0·612	0·299
	0·80	1·737	1·445	0·617	1·013	0·187	0·638	0·422
	0·85	1·777	1·367	0·634	1·051	0·081	0·650	0·524

TABLE 7

Calculated Theoretical Pitching Derivatives for Unswept Tapered Wing

(a) *Free stream (Table 4)*

$x_0/\bar{c}$	M	l_θ	$l_{\dot{\theta}}$	m_θ	$-m_{\dot{\theta}}$	l_q	$-m_q$
0·395	0	1·926	1·138	−0·210	0·584	1·316	0·381
	0·6	2·168	0·937	−0·227	0·746	1·490	0·447
	0·8	2·466	0·528	−0·242	1·055	1·713	0·539
1·185	0	1·926	−0·383	1·312	0·721	−0·205	0·377
	0·6	2·168	−0·776	1·485	1·179	−0·222	0·443
	0·8	2·466	−1·420	1·706	1·986	−0·235	0·534

(b) *Slotted tunnel with variable porosity*

M	$1/P_E$	$l_{\theta T}$	$x_0 = 0{\cdot}395\bar{c}$			$x_0 = 1{\cdot}185\bar{c}$		
			$l_{\dot{\theta}T}$	$-m_{\theta T}$	$-m_{\dot{\theta}T}$	$-l_{\dot{\theta}T}$	$m_{\theta T}$	$-m_{\dot{\theta}T}$
0	∞	2·033	1·113	0·226	0·584	0·493	1·380	0·795
	3·0	1·985	1·104	0·222	0·575	0·465	1·346	0·766
	1·0	1·916	1·220	0·213	0·583	0·294	1·301	0·647
	0·4	1·857	1·365	0·203	0·601	0·102	1·264	0·521
	0	1·793	1·504	0·192	0·622	0·087	1·225	0·402
0·6	∞	2·314	0·851	0·252	0·746	0·976	1·576	1·319
	3·0	2·254	0·840	0·247	0·725	0·941	1·534	1·273
	1·0	2·165	1·043	0·235	0·732	0·667	1·475	1·073
	0·4	2·085	1·303	0·221	0·762	0·344	1·426	0·860
	0	1·997	1·554	0·204	0·799	0·023	1·374	0·656
0·8	∞	2·676	0·310	0·280	1·070	1·804	1·834	2·273
	3·0	2·604	0·262	0·277	1·005	1·795	1·780	2·205
	1·0	2·483	0·626	0·260	0·995	1·336	1·701	1·845
	0·4	2·368	1·131	0·238	1·051	0·740	1·632	1·447
	0	2·236	1·631	0·208	1·123	0·136	1·558	1·066

TABLE 8

Uncorrected Experimental Pitching Derivatives for Unswept Tapered Wing

Hole size	M	$l_{\theta T}$	$x_0 = 0{\cdot}395\bar{c}$			$x_0 = 1{\cdot}185\bar{c}$		
			$l_{\dot{\theta} T}$	$-m_{\theta T}$	$-m_{\dot{\theta} T}$	$-l_{\dot{\theta} T}$	$m_{\theta T}$	$-m_{\dot{\theta} T}$
0 (slots sealed)	0·406	1·897	0·987	0·234	0·616	0·512	1·265	0·836
	0·510	1·972	0·892	0·232	0·622	0·666	1·326	0·965
	0·616	2·104	0·795	0·256	0·662	0·867	1·406	1·145
	0·718	2·248	0·668	0·265	0·736	1·108	1·514	1·402
	0·823	2·470	0·283	0·301	0·856	1·668	1·650	1·936
	0·886	2·634	−0·339	0·415	0·917	2·420	1·666	2·501
0·06 in 1·6 mm	0·608	2·086	0·812	0·252	0·648	0·836	1·396	1·109
	0·812	2·347	0·324	0·289	0·832	1·530	1·565	1·812
0·31 in 7·9 mm	0·608	1·983	1·204	0·237	0·697	0·362	1·329	0·796
	0·812	2·262	0·976	0·265	0·911	0·811	1·522	1·342
Slots open	0·405	1·704	1·509	0·195	0·619	−0·163	1·151	0·336
	0·507	1·781	1·526	0·205	0·646	−0·089	1·202	0·414
	0·609	1·864	1·425	0·212	0·682	−0·047	1·260	0·552
	0·710	1·933	1·375	0·220	0·769	−0·152	1·307	0·715
	0·813	2·071	1·168	0·253	0·889	−0·468	1·383	1·059
	0·865	2·243	0·975	0·303	1·014	−0·797	1·469	1·404

TABLE 9

Corrected Experimental Pitching Derivatives for Unswept Tapered Wing

Slots	M	l_{θ}	$x_0 = 0{\cdot}395\bar{c}$			$x_0 = 1{\cdot}185\bar{c}$		
			$l_{\dot{\theta}}$	$-m_{\theta}$	$-m_{\dot{\theta}}$	$-l_{\dot{\theta}}$	m_{θ}	$-m_{\dot{\theta}}$
Sealed $\frac{1}{P_E} = \infty$	0·406	1·800	1·010	0·217	0·615	0·426	1·207	0·781
	0·510	1·866	0·929	0·213	0·624	0·559	1·262	0·896
	0·616	1·981	0·852	0·234	0·665	0·727	1·333	1·056
	0·718	2·103	0·754	0·238	0·741	0·923	1·426	1·283
	0·823	2·285	0·448	0·263	0·868	1·378	1·546	1·750
	0·886	2·414	−0·055	0·361	0·946	1·992	1·556	2·248
Open $\frac{1}{P_E} = 0$	0·405	1·825	1·155	0·213	0·578	0·268	1·228	0·622
	0·507	1·915	1·106	0·225	0·598	0·425	1·287	0·755
	0·609	2·013	0·891	0·235	0·622	0·682	1·354	0·974
	0·710	2·098	0·698	0·246	0·695	0·936	1·409	1·238
	0·813	2·269	0·157	0·288	0·773	1·607	1·501	1·809
	0·865	2·483	−0·465	0·349	0·834	2·405	1·607	2·441

TABLE 10

Practical Estimates of Interference-Free Pitching Derivatives for Cropped Delta Wing ($x_0 = 1{\cdot}039\bar{c}$)

Experiment	Method	M	l_θ	$l_{\dot\theta}$	m_θ	$-m_{\dot\theta}$
With optimum wall porosity	Section 5	0·6	1·53	0·46	0·59	0·19
		0·8	1·62	0·31	0·63	0·36
With open and sealed slots	Ref. 1, eq. (58)	0·6	1·55	0·42	0·58	0·21
		0·8	1·68	0·24	0·63	0·41
In ventilated large tunnels	Ref. 3, Fig. 8	0·6	1·55	0·35	0·56	0·22
		0·8	1·67	0·20	0·62	0·41

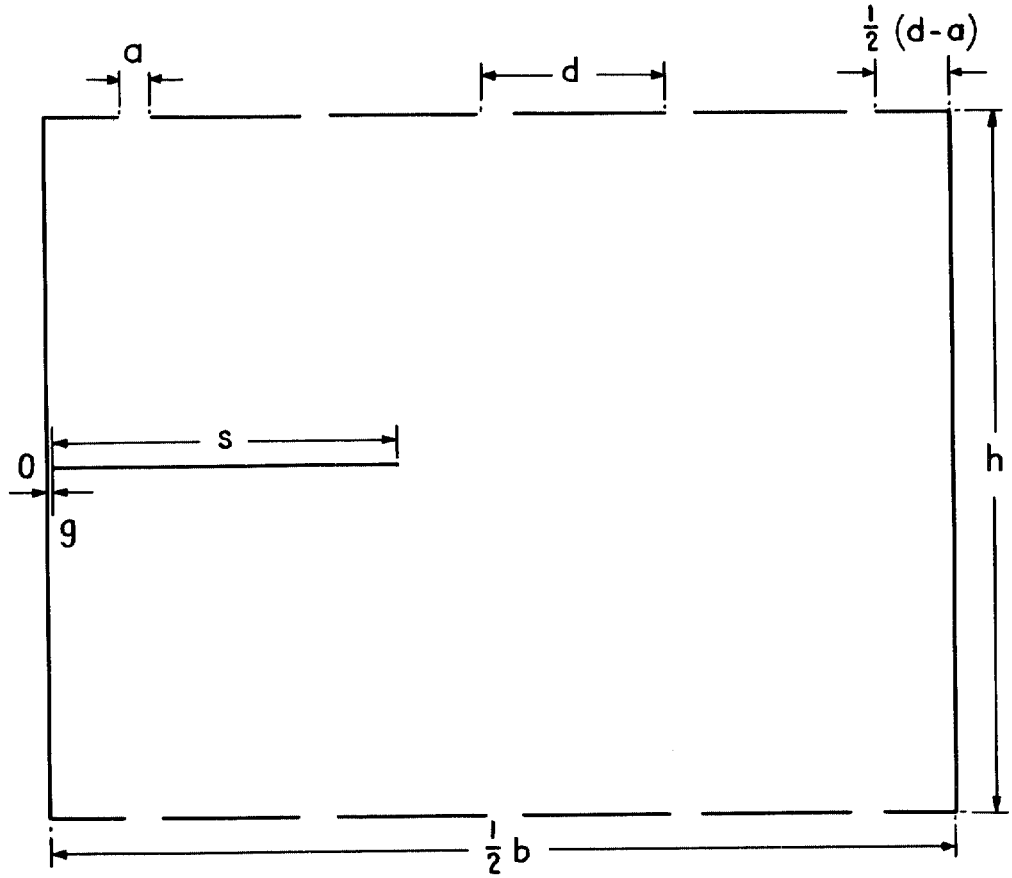

Effective tunnel breadth	b = 19 in (482 mm)
Height of tunnel	h = 7·30 in (185 mm)
Regular slot spacing	d = 1·9 in (48 mm)
Width of each slot	a = 0·3 in (7·6 mm)
Span of half model	s = 3·60 in (91·5 mm)
Gap at side-wall	g = 0·05 in (1·3 mm)

$$b/h = 2{\cdot}6\,, \quad F = 0{\cdot}233\,, \quad \sigma = 2\,(s+g)/b = 0{\cdot}385$$

FIG. 1. Working section of tunnel with five wide slots in roof and floor.

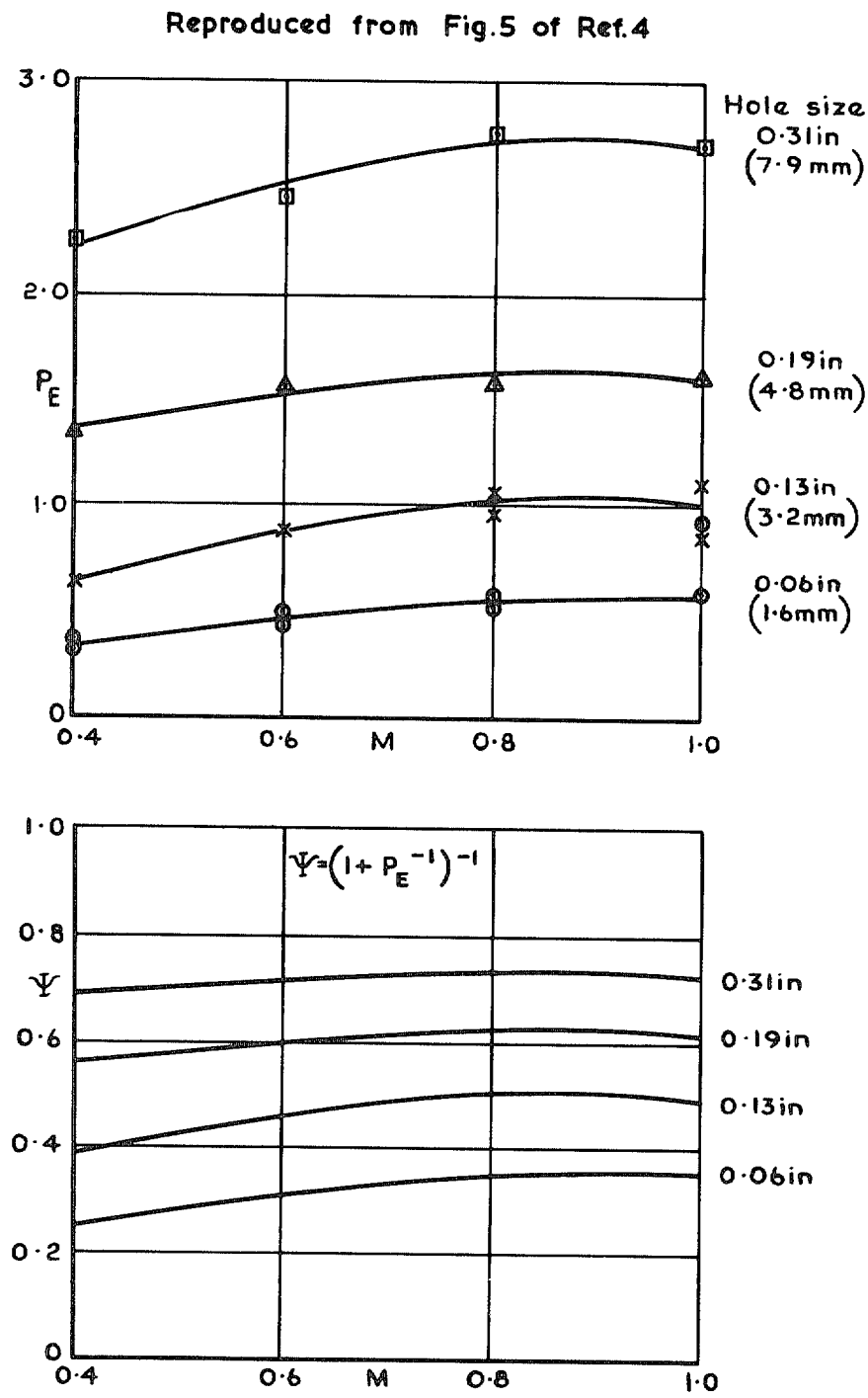

FIG. 2. Porosity parameters for the slotted walls with variably perforated screens over a range of Mach number.

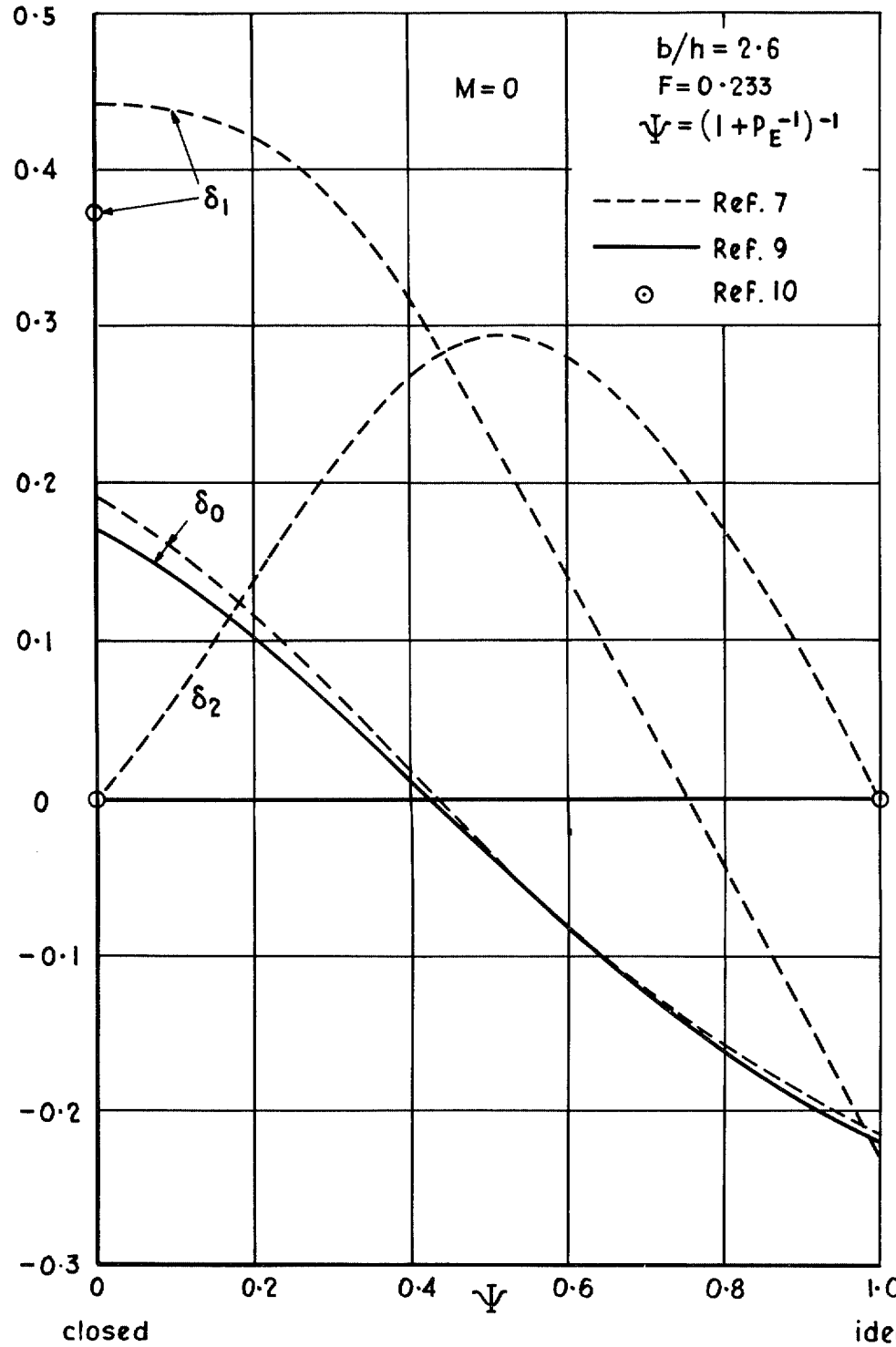

FIG. 3. Steady interference parameters for small wings in tunnel with roof and floor of varying porosity.

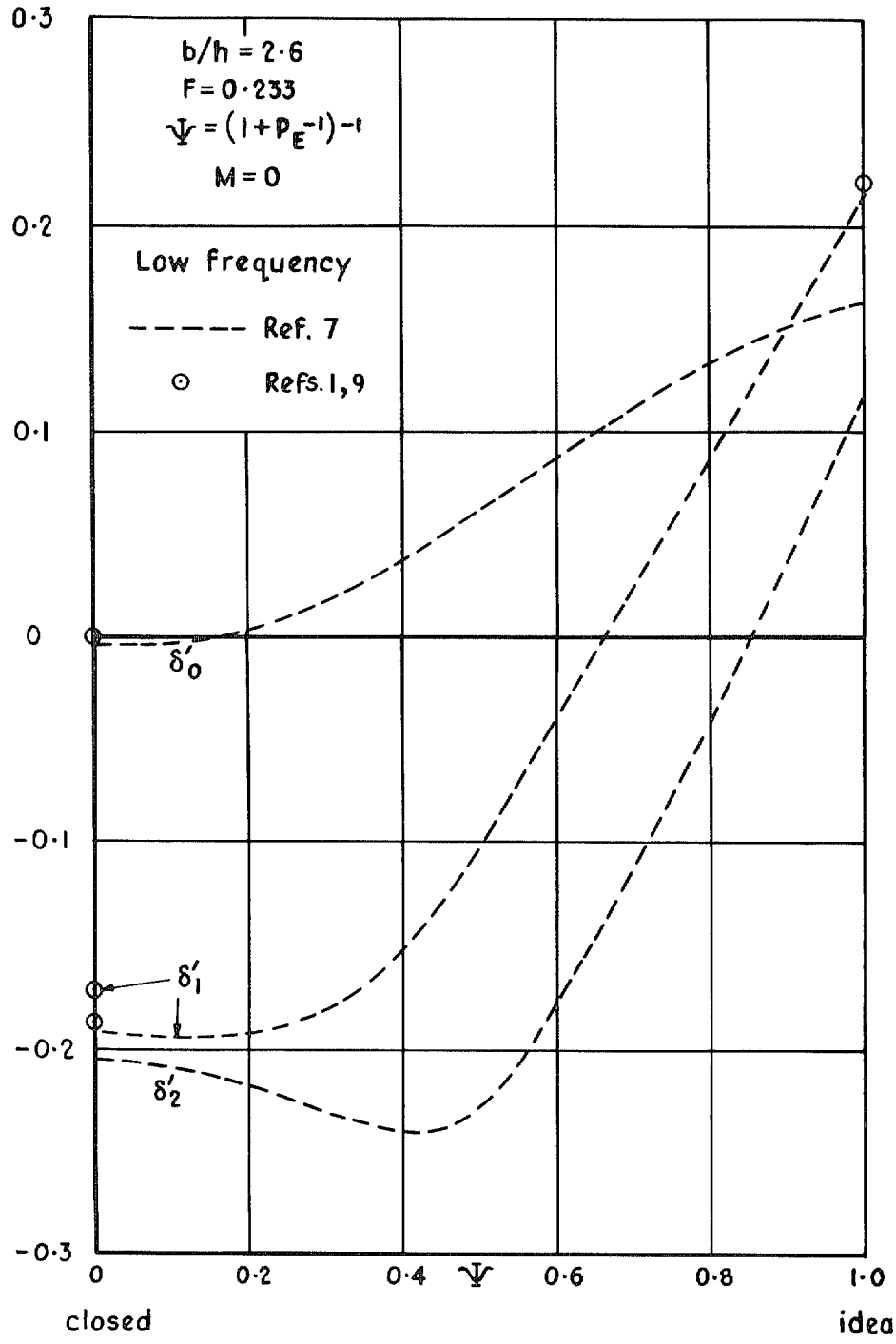

FIG. 4. Additional unsteady interference parameters for small wings in slotted tunnel of varying porosity.

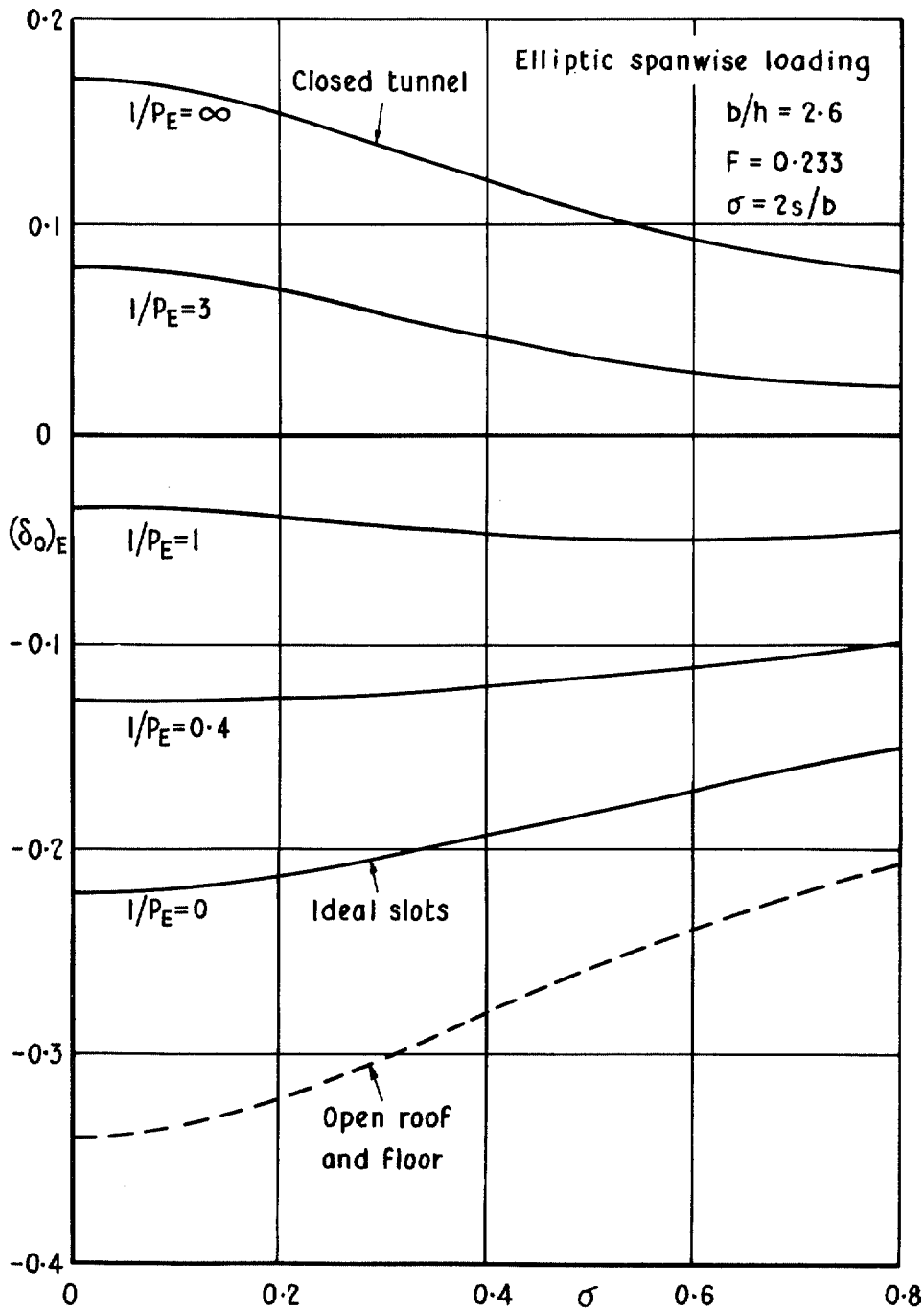

FIG. 5. Effect of wing span on steady lift interference in tunnel with slotted roof and floor of variable porosity.

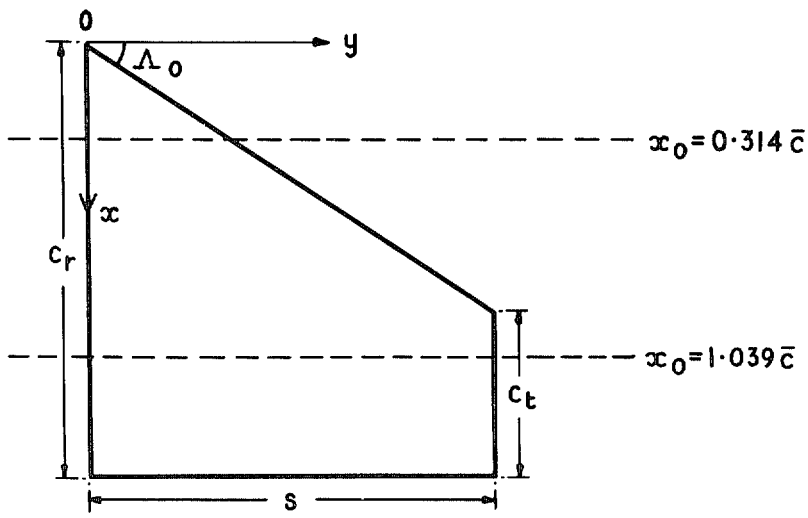

$c_r = 1{\cdot}44\,\bar{c}$ $\quad \tan\Lambda_0 = 0{\cdot}6$ $\quad \bar{c} = 3{\cdot}927\text{in}$

$c_t = 0{\cdot}56\,\bar{c}$ $\quad s = 1{\cdot}32\,\bar{c}$ $\quad = 99{\cdot}7\text{ mm}$

a Cropped delta wing (A = 2·64)

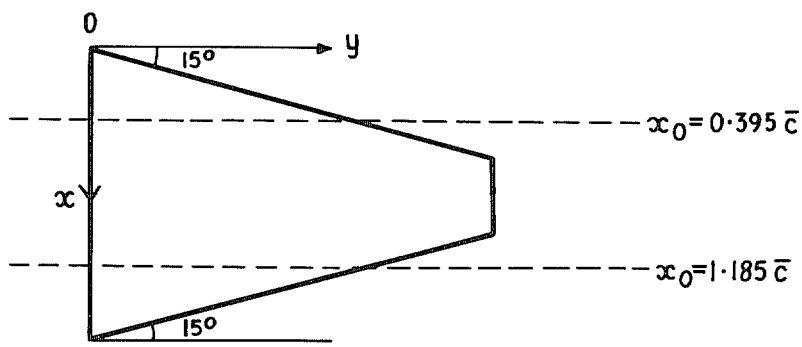

$c_r = 1{\cdot}5800\,\bar{c}$ $\quad \Lambda_0 = 15°$ $\quad \bar{c} = 2{\cdot}628\text{in}$

$c_t = 0{\cdot}4200\,\bar{c}$ $\quad s = 2{\cdot}1646\,\bar{c}$ $\quad = 66{\cdot}7\text{ mm}$

b Unswept tapered wing (A = 4·3292)

FIG. 6a and b. Definitions of planforms and locations of pitching axes.

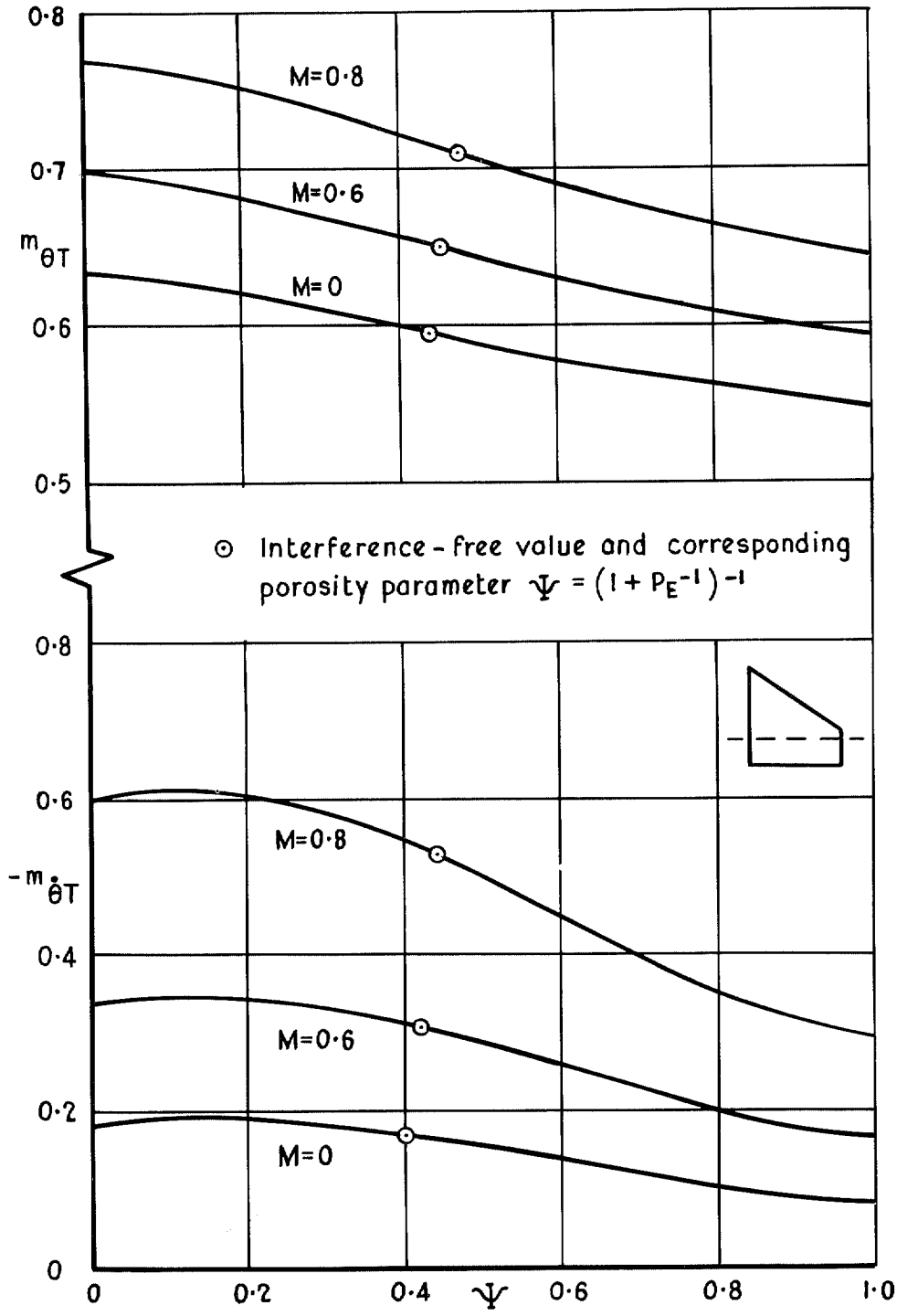

FIG. 7. Theoretical effect of wall porosity on aerodynamic stiffness and damping of cropped delta wing in pitching oscillation.

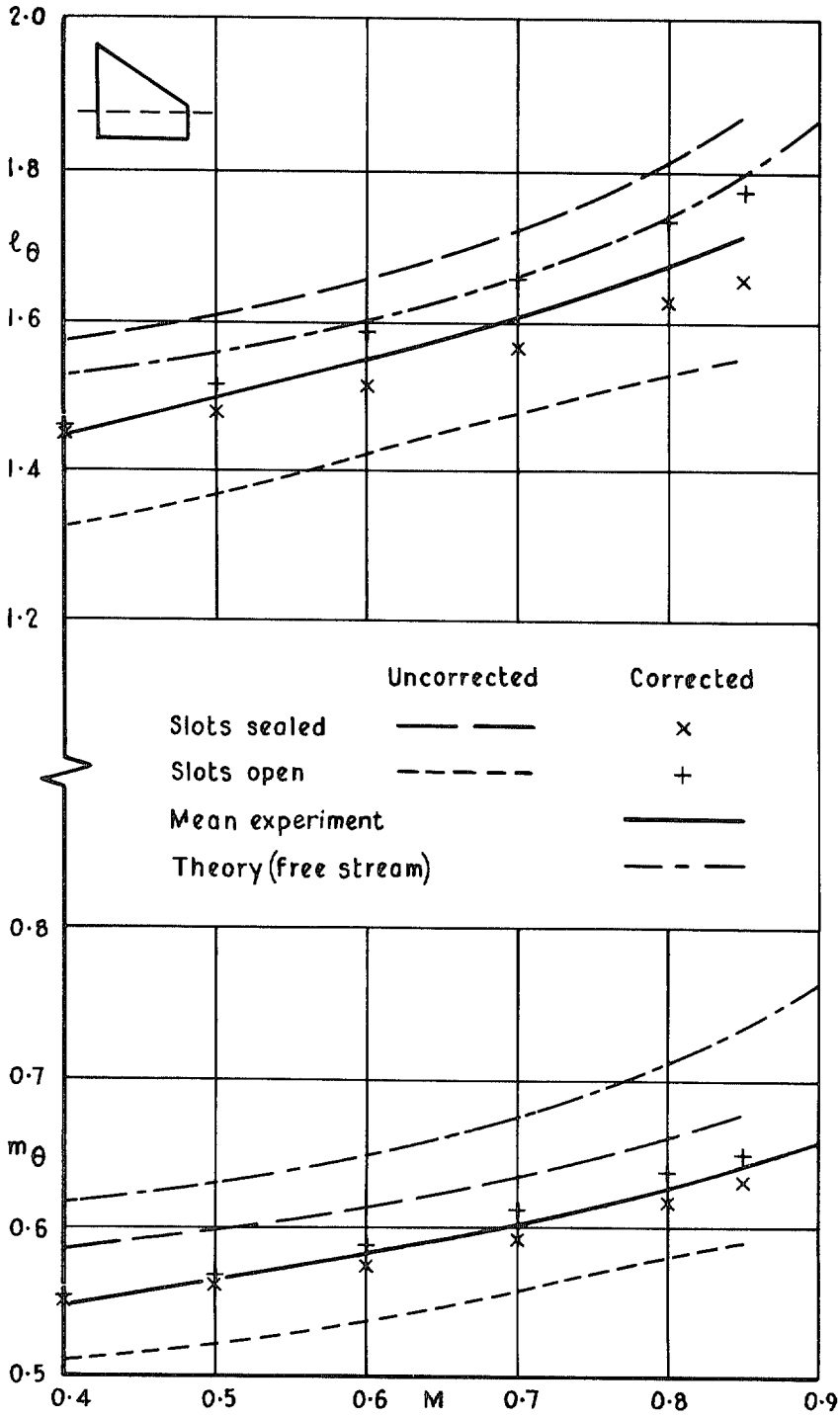

FIG. 8. Corrections to l_θ and m_θ against Mach number for cropped delta wing under two wall conditions.

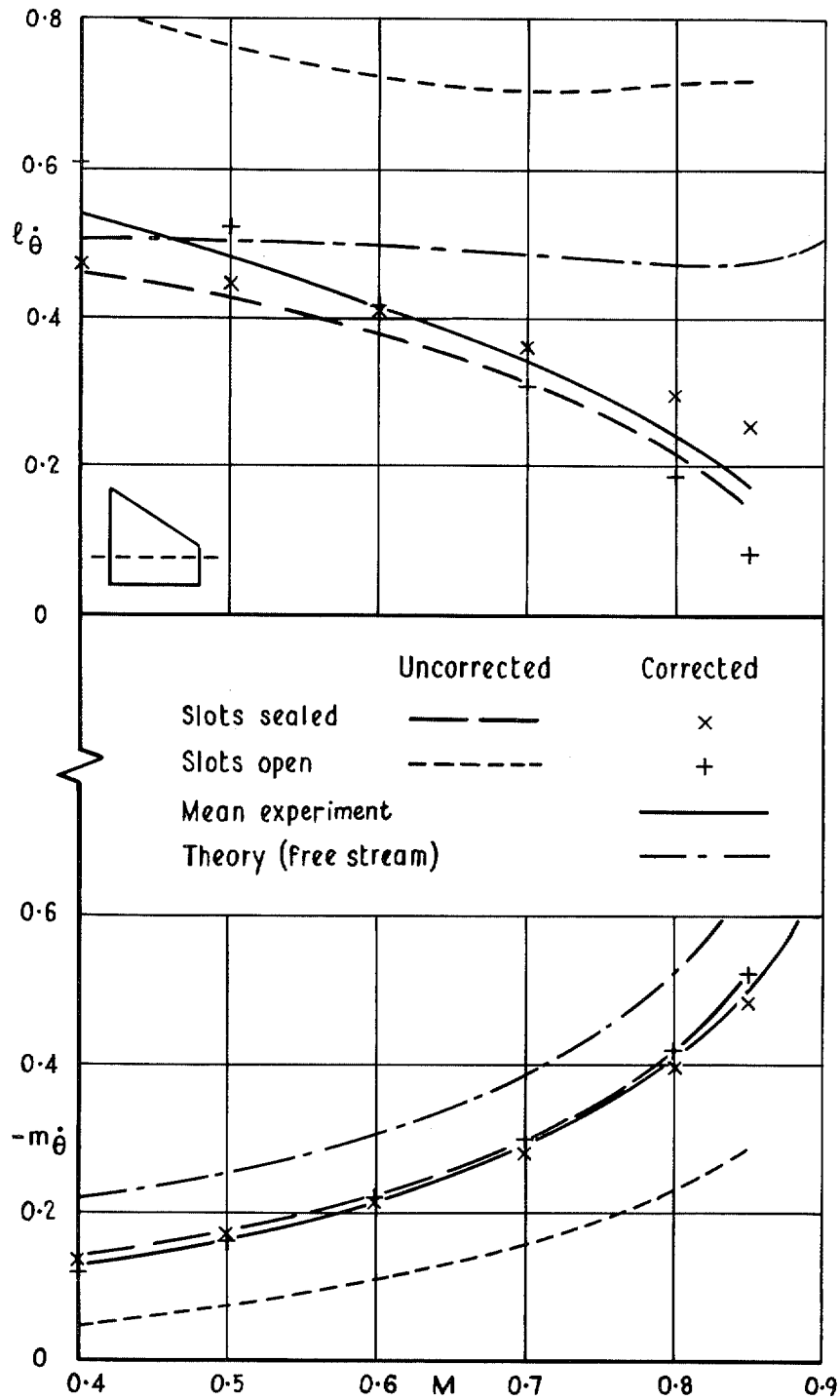

FIG. 9. Corrections to $l_{\dot{\theta}}$ and $-m_{\dot{\theta}}$ against Mach number for cropped delta wing under two wall conditions.

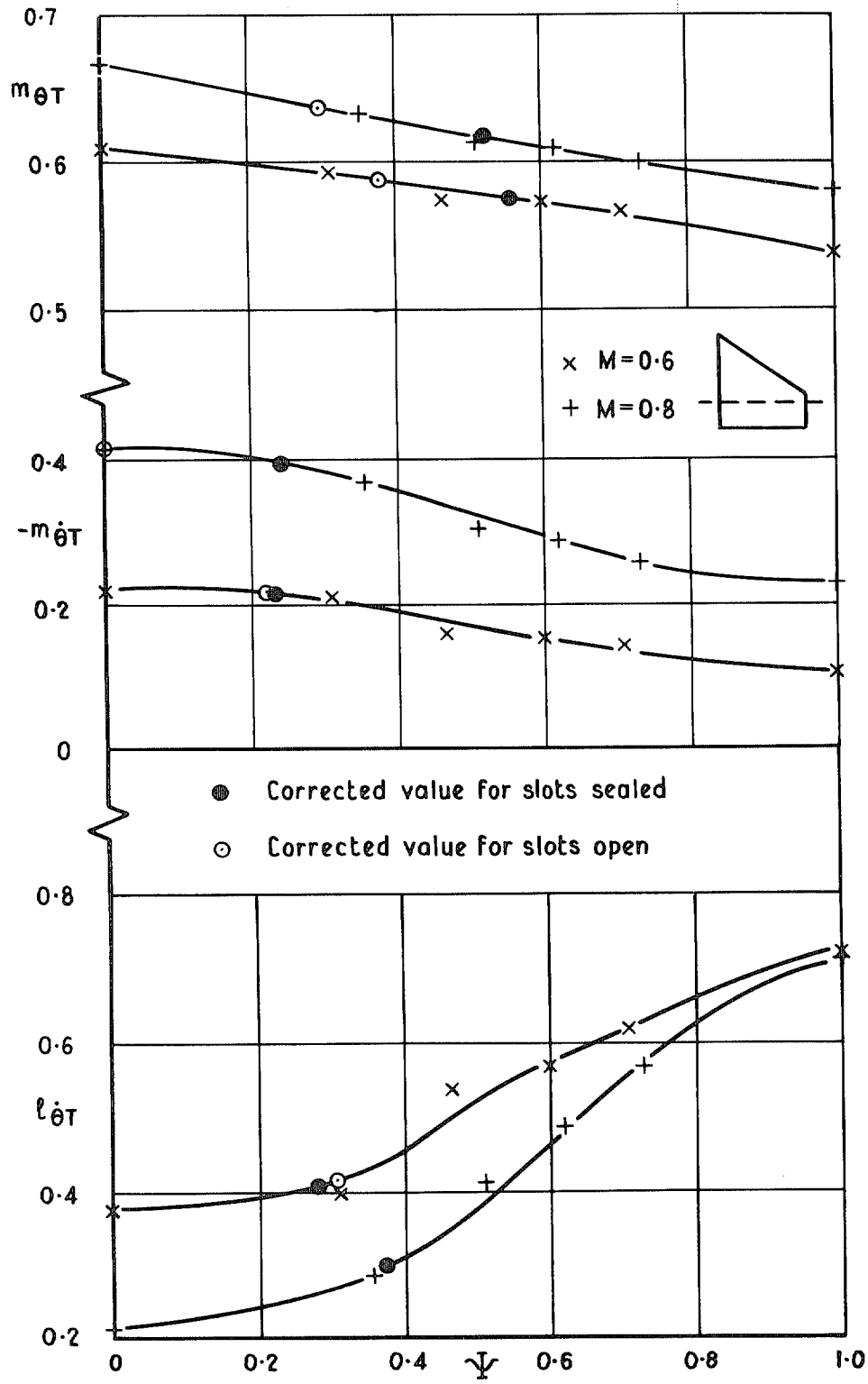

FIG. 10. Measured effect of wall porosity on pitching derivatives of cropped delta wing at two Mach numbers.

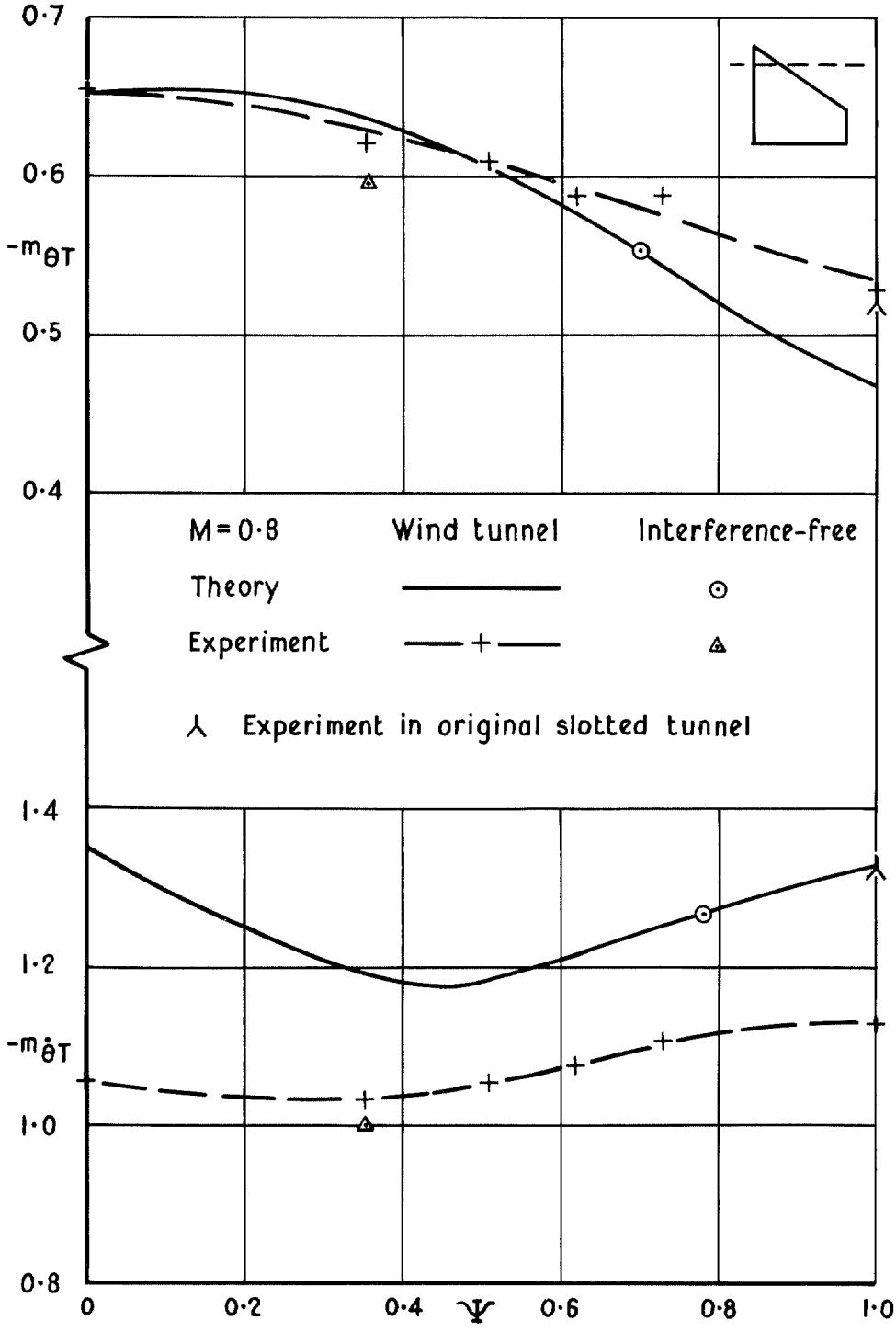

FIG. 11. Theoretical and experimental effects of wall porosity on $-m_\theta$ and $-m_{\dot{\theta}}$ for cropped delta wing ($x_0 = 0{\cdot}314\bar{c}$).

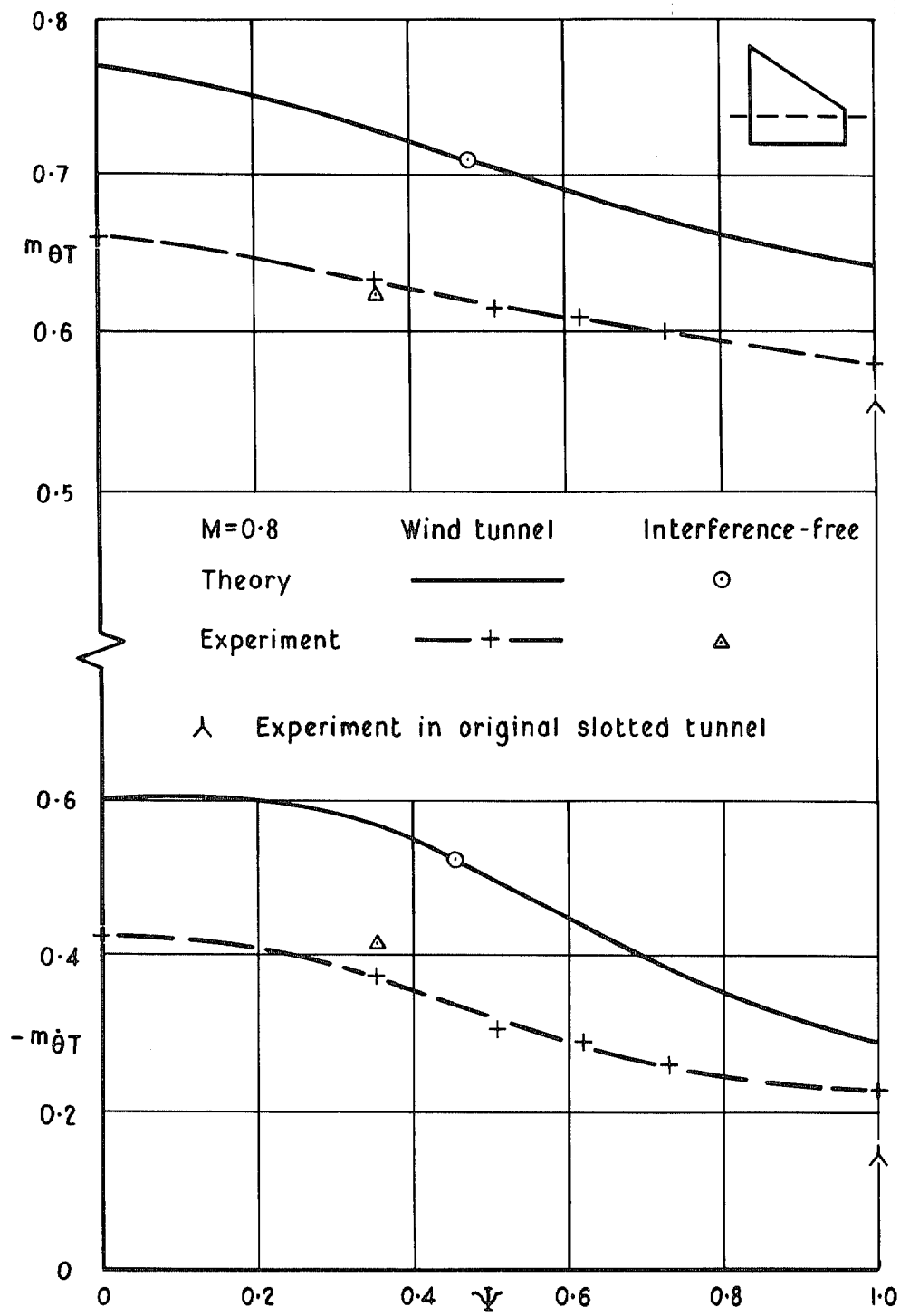

FIG. 12. Theoretical and experimental effects of wall porosity on m_θ and $-m_{\dot{\theta}}$ for cropped delta wing ($x_0 = 1{\cdot}039\bar{c}$).

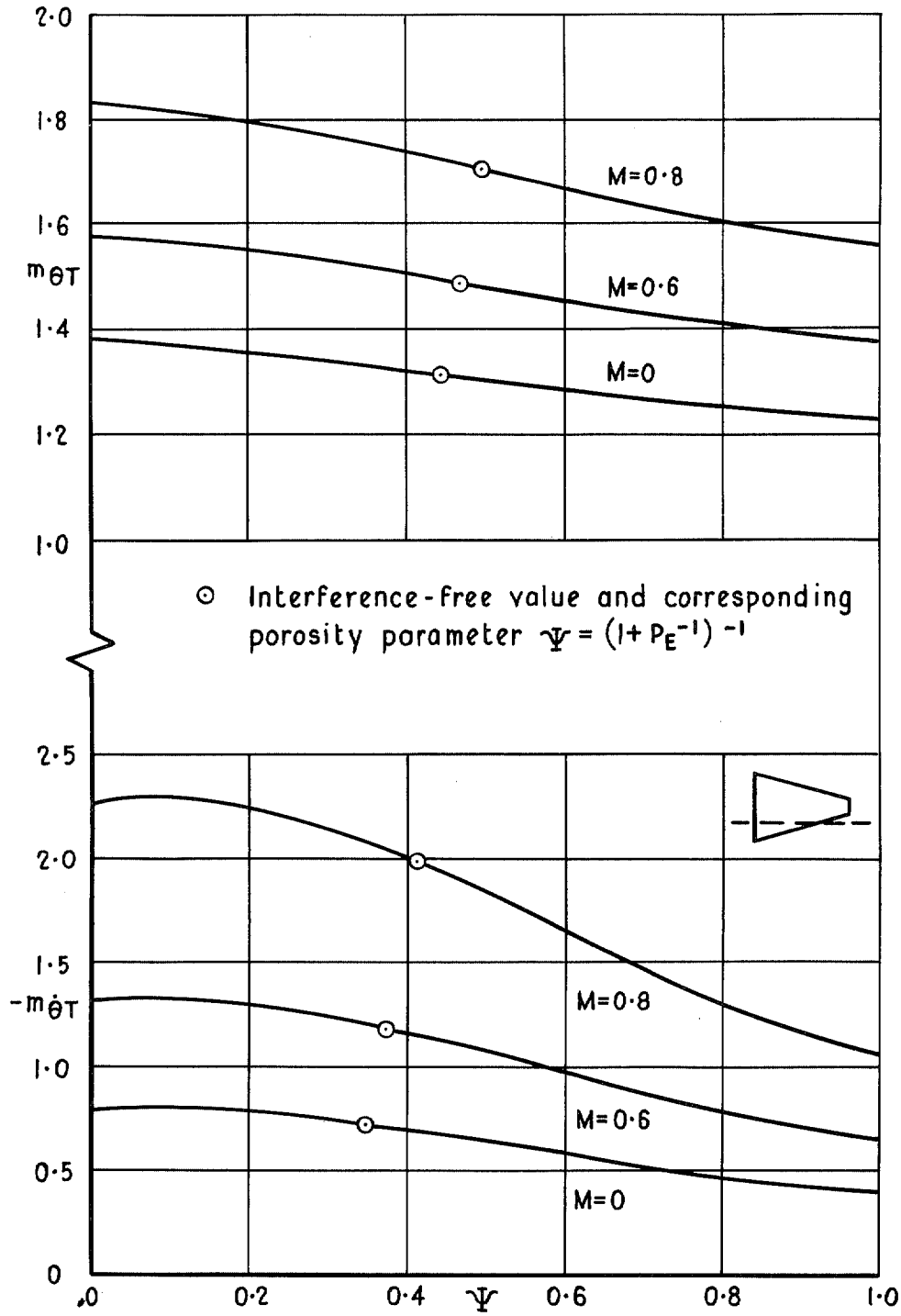

FIG. 13. Theoretical effect of wall porosity on aerodynamic stiffness and damping of unswept tapered wing in pitching oscillation.

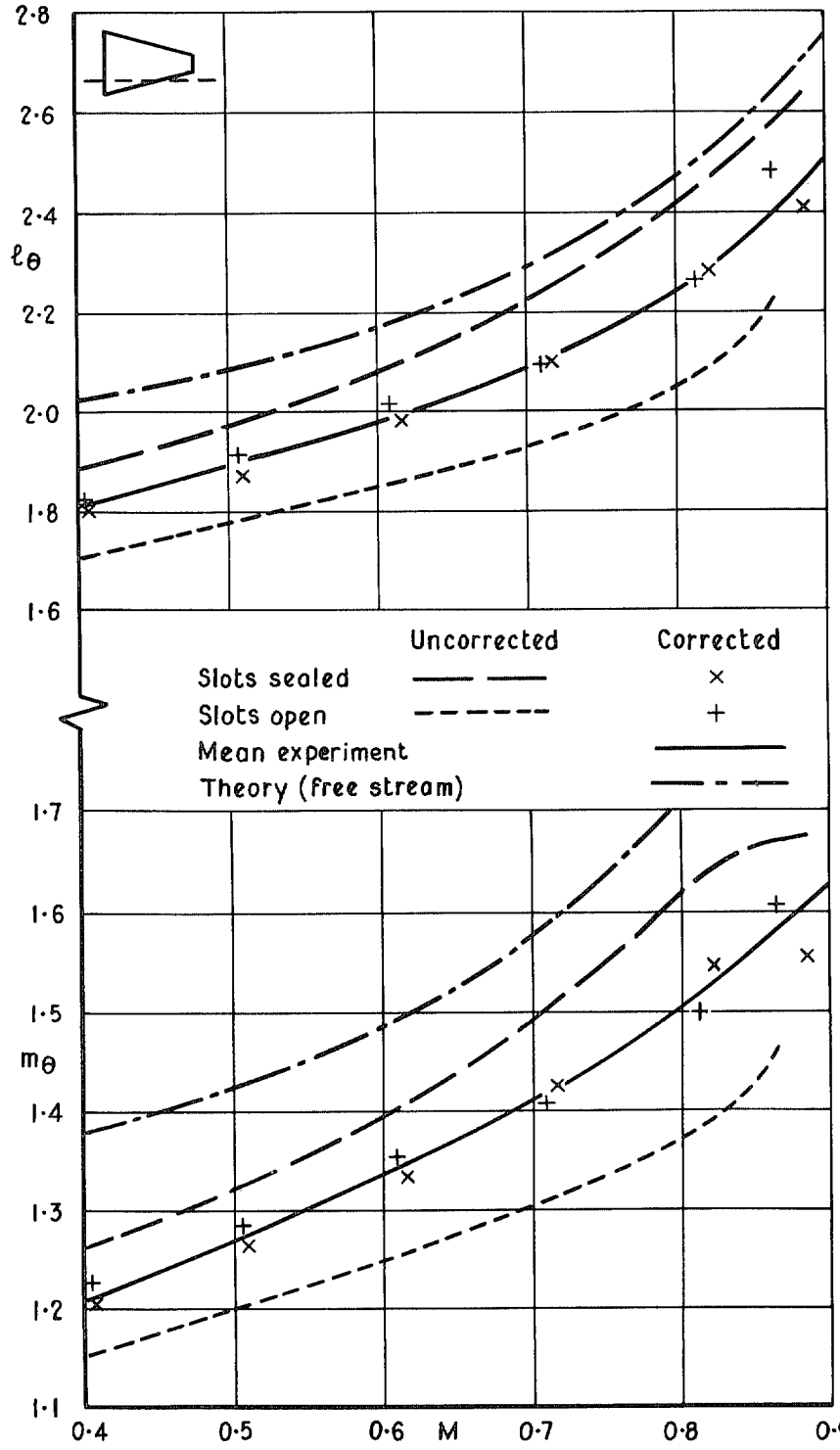

FIG. 14. Corrections to l_θ and m_θ against Mach number for unswept tapered wing under two wall conditions.

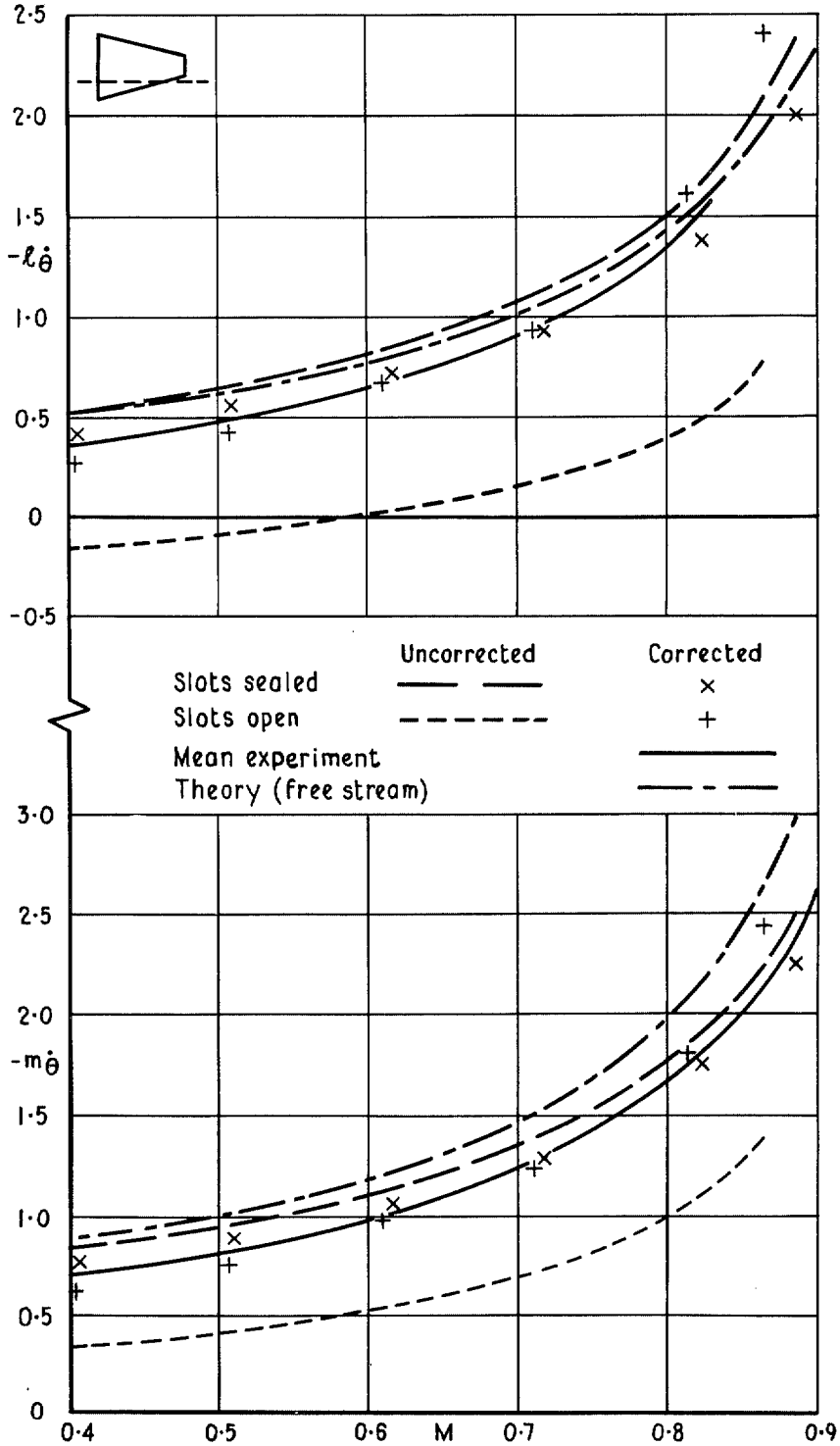

FIG. 15. Corrections to $-l_{\dot{\theta}}$ and $-m_{\dot{\theta}}$ against Mach number for unswept tapered wing under two wall conditions.

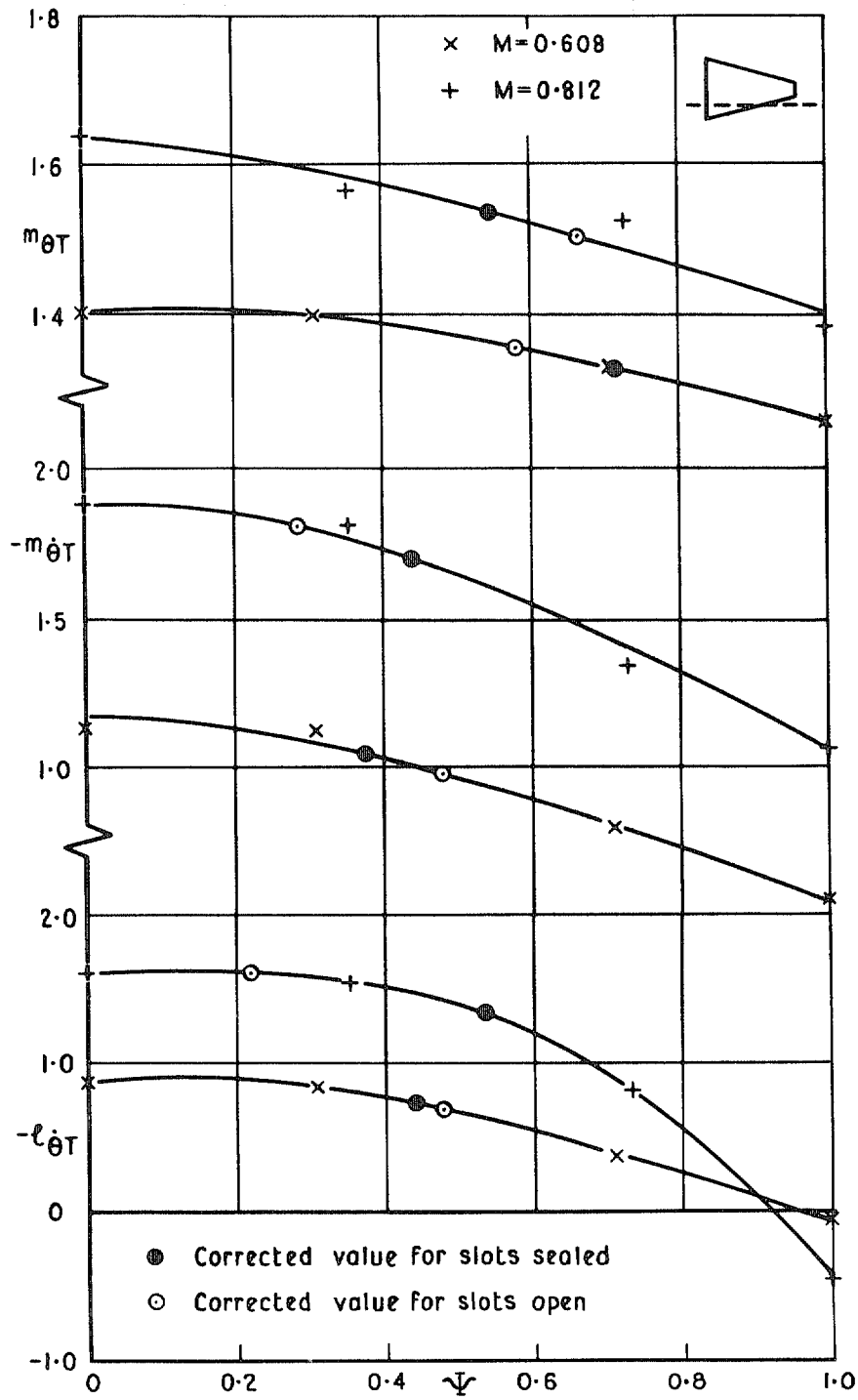

FIG. 16. Measured effect of wall porosity on pitching derivatives of unswept tapered wing at two Mach numbers.

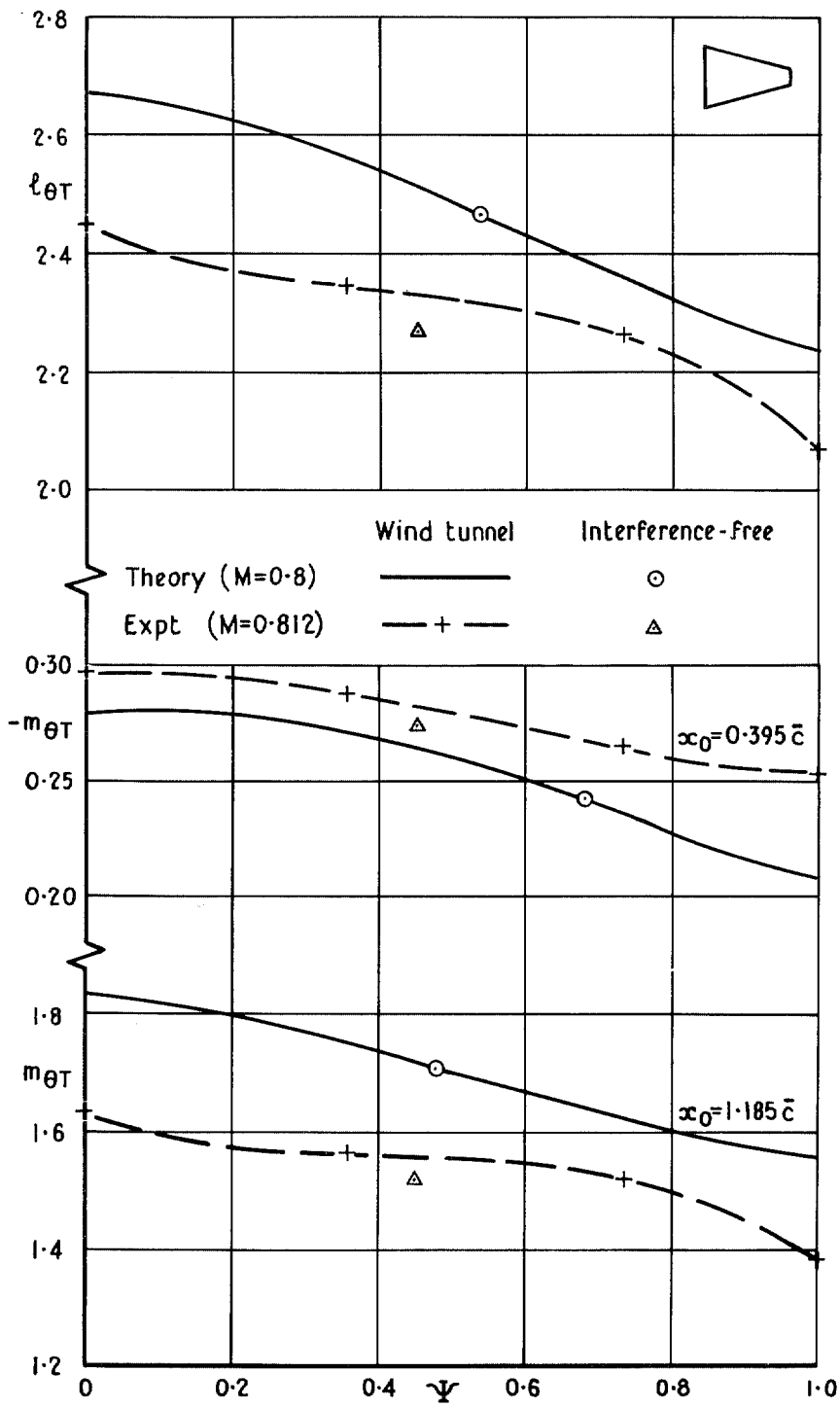

FIG. 17. Theoretical and experimental effects of wall porosity on stiffness derivatives of unswept tapered wing.

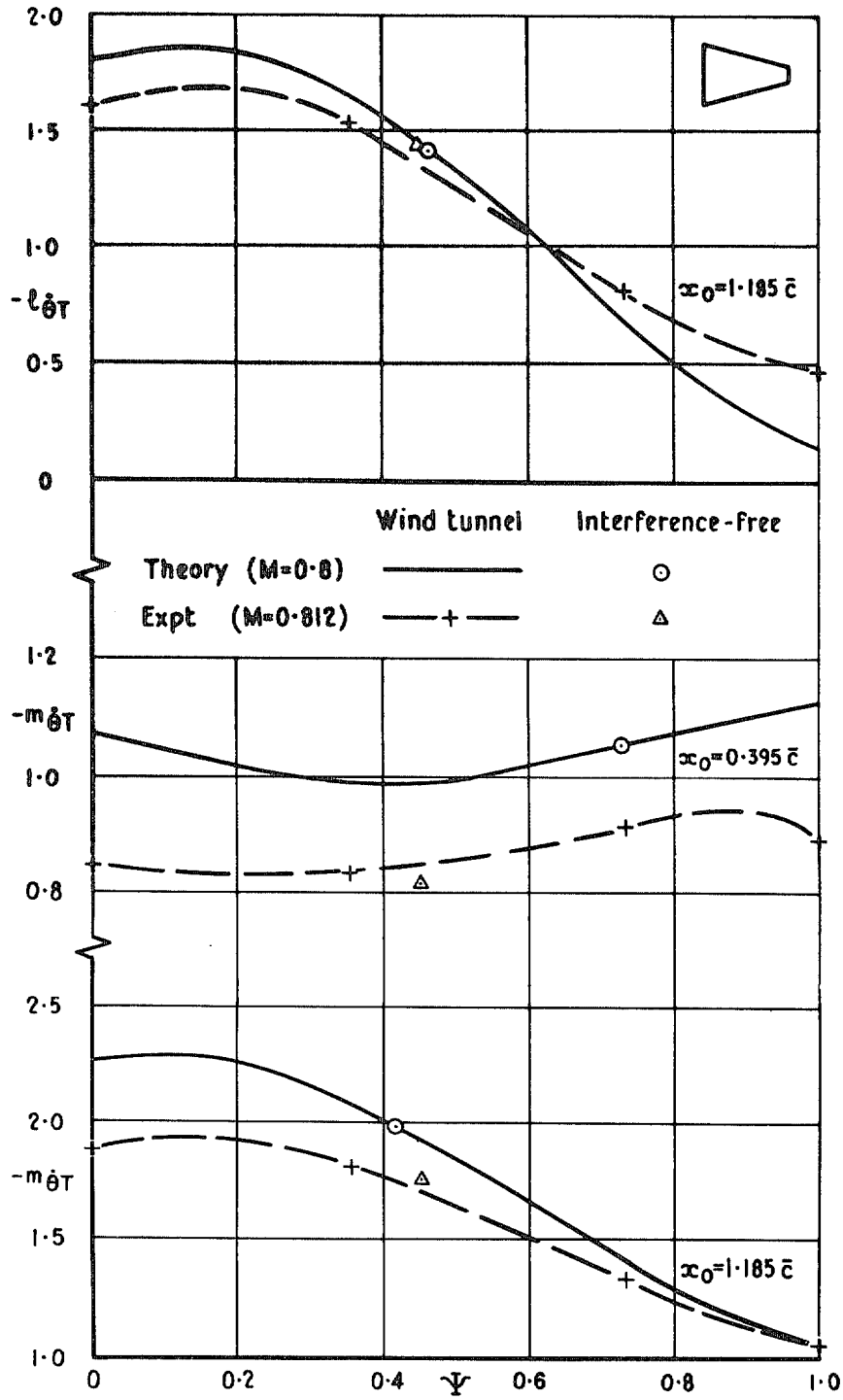

FIG. 18. Theoretical and experimental effects of wall porosity on damping derivatives of unswept tapered wing.

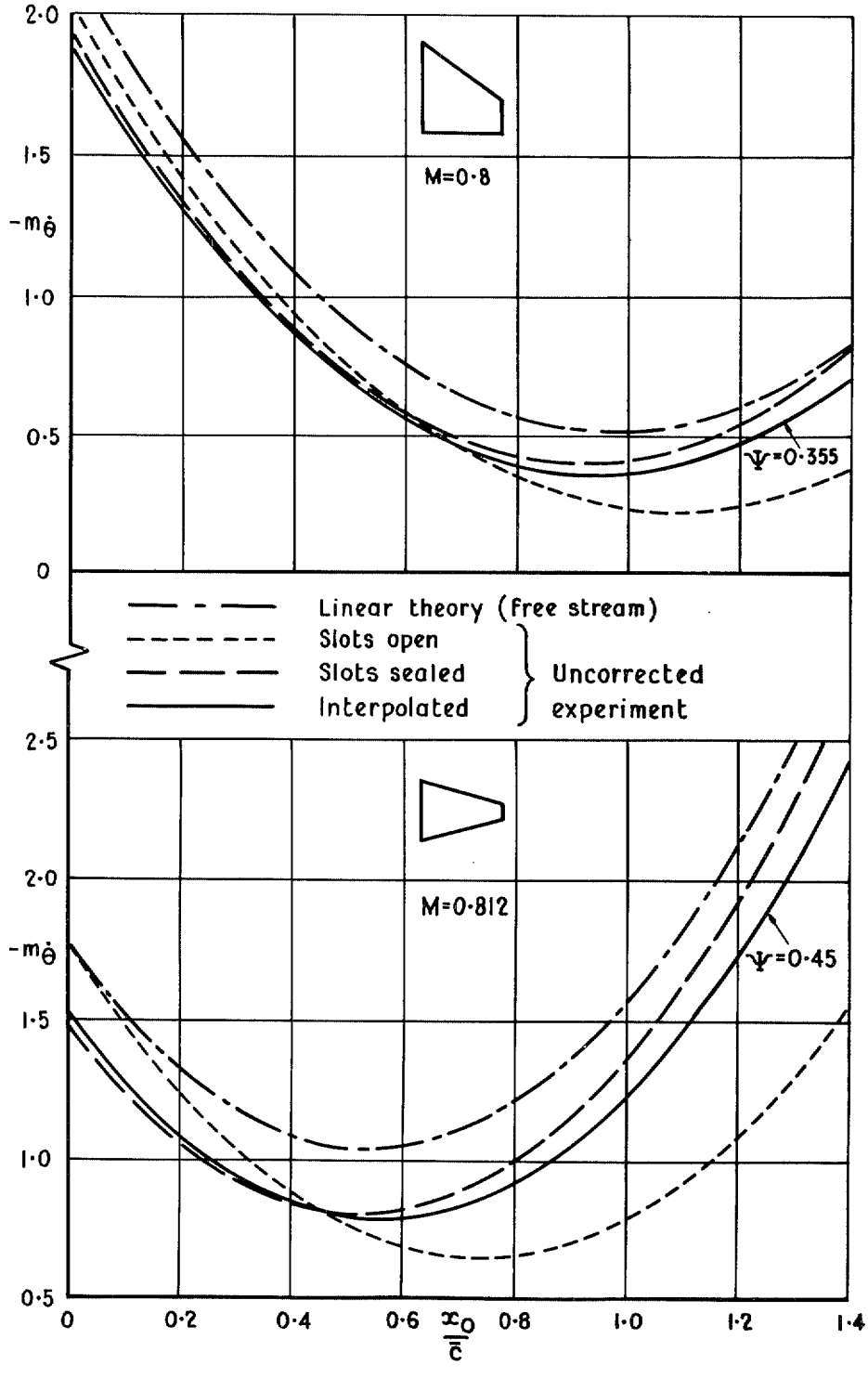

FIG. 19. Pitching damping against axis position as measured and calculated for two wings in high subsonic flow.

Printed in England for Her Majesty's Stationery Office by J. W. Arrowsmith Ltd., Bristol
Dd. 503426 K.5 8/72

HER MAJESTY'S STATIONERY OFFICE

Government Bookshops

49 High Holborn, London WC1V 6HB
13a Castle Street, Edinburgh EH2 3AR
109 St Mary Street, Cardiff CF1 1JW
Brazennose Street, Manchester M60 8AS
50 Fairfax Street, Bristol BS1 3DE
258 Broad Street, Birmingham B1 2HE
80 Chichester Street, Belfast BT1 4JY

Government publications are also available through booksellers

R. & M. No. 3706

SBN 11 470506 2